Long-range and local circuits for top-down modulation of visual cortex processing

Siyu Zhang *et al.*

This copy is for your personal, non-commercial use only.

and the bosonic field, v is the quartic coupling among the bosonic fields, λ is the linear coupling between the bosonic field and the orthorhombic lattice distortion ϵ, and $\mathbf{q}$ is the momentum transfer within one Brillouin zone. Minimizing the action with respect to ϵ, we arrive at $\epsilon = \lambda \langle \Delta \rangle / C_s$, where C_s is the shear modulus. In other words, the orthorhombic lattice distortion is proportional to the nematic order parameter $\langle \Delta \rangle$, and both are expected to develop nonzero expectation values below T_s (12–14). However, the nematic field Δ undergoes fluctuations in the tetragonal phase above T_s while lattice distortion ϵ remains zero. These fluctuations will be observable in dynamic quantities, such as the finite-energy spin fluctuations, and in transport measurements. We therefore conclude that the scale T^*, below which we observe anisotropy of low-energy spin fluctuations (Figs. 3E, 4E, and 4F) and where the resistivity anisotropy is observed (Fig. 3E, right inset), marks a typical range of the nematic fluctuations.

Several remarks are in order. First, the applied uniaxial pressure used to detwin the samples will induce a finite value of ϵ at any temperature, so that strictly speaking, the structural transition at T_s will be rendered a crossover. In practice, however, the applied pressure is too small to cause a perceptible lattice distortion, which is why the transition temperature T_s, as determined from the extinction effect of the nuclear $(2, -2, 0)$ Bragg peak remains unchanged from the zero-pressure case [fig. S2, B and D] (26, 27). On the other hand, the extent of nematic fluctuations may be sensitive to the shear strain, in agreement with the reported increase of T^* (as determined from resistivity anisotropy) with the uniaxial pressure (37). Second, in Eq. 1 the variable Δ could equally signify the orbital order $\Delta \propto (n_{xz} - n_{yz})$ which lifts the degeneracy between the Fe d_{xz} and d_{yz} orbitals. In fact, the two order parameters will couple linearly to each other, $\left(\mathbf{M}_1 \cdot \mathbf{M}_2 \right) \propto (n_{xz} - n_{yz})$, so that both will develop a nonzero value below T_s. In this respect, our findings are also consistent with the recent ARPES finding of an orbital ordering (17, 18) in BaFe$_2$As$_2$. This underlines the complementarity of the spin-nematic and orbital descriptions of the C_4 symmetry breaking. Third, in the nearly optimally electron-doped superconductor, we observe anisotropy of the low-lying spin excitations in the tetragonal phase $T_s < T < T^*$, even though the orbital order is no longer detectable by ARPES (17, 18). This is consistent with the absence of a static nematic order $\langle \Delta \rangle = 0$ above T_s, whereas the observed spin anisotropy originates from Ising-nematic fluctuations. Because T_s is considerably suppressed for this doping, these fluctuations are quantum rather than thermal: They persist beyond the immediate vicinity of T_s, and the associated spin anisotropy should have sizable dependence on frequency that can be probed by future experiments. Fourth, when resistivity anisotropy under uniaxial strain disappears in the electron-overdoped sample (10), the uniaxial-strain–induced spin excitation anisotropy also vanishes (Fig. 1E and fig. S5), which suggests a direct connection between these two phenomena.

Finally, our measurements in the spin channel do not necessarily signal a thermodynamic order at the temperature T^*. Rather, T^* likely signals a crossover, whereas the true nematic transition occurs at T_s (9). This implies that a static order above T_s inferred from recent measurements of magnetic torque anisotropy in the isovalent BaFe$_2$As$_{2-x}$P$_x$ (38) is most likely not in the spin channel accessible to the inelastic neutron scattering. A static order in other channels—such as, for instance, an octupolar order—would, however, not contradict our observations.

REFERENCES AND NOTES

1. Y. Kamihara, T. Watanabe, M. Hirano, H. Hosono, *J. Am. Chem. Soc.* **130**, 3296–3297 (2008).
2. G. R. Stewart, *Rev. Mod. Phys.* **83**, 1589–1652 (2011).
3. P. C. Dai, J. Hu, E. Dagotto, *Nat. Phys.* **8**, 709–718 (2012).
4. C. de la Cruz, Q. Huang, J. W. Lynn, J. Li, W. Ratcliff II J. L. Zarestky et al., *Nature* **453**, 899–902 (2008).
5. Q. Huang et al., *Phys. Rev. Lett.* **101**, 257003 (2008).
6. M. G. Kim et al., *Phys. Rev. B* **83**, 134522 (2011).
7. J. H. Chu et al., *Science* **329**, 824–826 (2010).
8. M. A. Tanatar et al., *Phys. Rev. B* **81**, 184508 (2010).
9. J. H. Chu, H.-H. Kuo, J. G. Analytis, I. R. Fisher, *Science* **337**, 710–712 (2012).
10. I. R. Fisher, L. Degiorgi, Z. X. Shen, *Rep. Prog. Phys.* **74**, 124506 (2011).
11. E. Fradkin, S. A. Kivelson, M. J. Lawler, J. P. Eisenstein, A. P. Mackenzie, *Annu. Rev. Condens. Matter Phys.* **1**, 153–178 (2010).
12. R. M. Fernandes, A. V. Chubukov, J. Schmalian, *Nat. Phys.* **10**, 97–104 (2014).
13. C. Fang, H. Yao, W.-F. Tsai, J. P. Hu, S. A. Kivelson, *Phys. Rev. B* **77**, 224509 (2008).
14. J. Dai, Q. Si, J. X. Zhu, E. Abrahams, *Proc. Natl. Acad. Sci. U.S.A.* **106**, 4118–4121 (2009).
15. M. P. Allan et al., *Nat. Phys.* **9**, 220–224 (2013).
16. S. Ishida et al., *Phys. Rev. Lett.* **110**, 207001 (2013).
17. M. Yi et al., *Proc. Natl. Acad. Sci. U.S.A.* **108**, 6878–6883 (2011).
18. Y. Zhang et al., *Phys. Rev. B* **85**, 085121 (2012).
19. C. C. Lee, W. G. Yin, W. Ku, *Phys. Rev. Lett.* **103**, 267001 (2009).
20. F. Krüger, S. Kumar, J. Zaanen, J. van den Brink, *Phys. Rev. B* **79**, 054504 (2009).
21. W. C. Lv, J. S. Wu, P. Phillips, *Phys. Rev. B* **80**, 224506 (2009).
22. C.-C. Chen et al., *Phys. Rev. B* **82**, 100504 (2010).
23. H. Luo et al., *Phys. Rev. Lett.* **108**, 247002 (2012).
24. X. Lu et al., *Phys. Rev. Lett.* **110**, 257001 (2013).
25. C. Dhital et al., *Phys. Rev. Lett.* **108**, 087001 (2012).
26. Yu. Song et al., *Phys. Rev. B* **87**, 184511 (2013).
27. Materials and methods are available as supplementary materials on *Science* Online.
28. C. Lester et al., *Phys. Rev. B* **79**, 144523 (2009).
29. A. Kreyssig et al., *Phys. Rev. B* **81**, 134512 (2010).
30. J. T. Park et al., *Phys. Rev. B* **86**, 024437 (2012).
31. L. W. Harriger et al., *Phys. Rev. B* **84**, 054544 (2011).
32. M. Nakajima et al., *Phys. Rev. Lett.* **109**, 217003 (2012).
33. M. Y. Wang et al., *Phys. Rev. B* **83**, 094516 (2011).
34. P. Chandra, P. Coleman, A. I. Larkin, *Phys. Rev. Lett.* **64**, 88–91 (1990).
35. R. M. Fernandes, J. Schmalian, *Supercond. Sci. Technol.* **25**, 084005 (2012).
36. The Ginzburg-Landau action up to the 4th power of $\mathbf{M}_{1/2}$: $S_0 \left[\mathbf{M}_1^2, \mathbf{M}_2^2 \right] = \iint d\mathbf{q} d\omega \, \left(r_0 + \mathbf{q}^2 + \gamma |\omega| \right) \left(\mathbf{M}_1^2 + \mathbf{M}_2^2 \right) + u \left(\mathbf{M}_1^2 + \mathbf{M}_2^2 \right)^2$, where $r_0 \propto T - T_N$ describes distance from the Néel point.
37. H.-H. Kuo et al., *Phys. Rev. B* **84**, 054540 (2011).
38. S. Kasahara et al., *Nature* **486**, 382–385 (2012).

SELECTIVE ATTENTION

Long-range and local circuits for top-down modulation of visual cortex processing

Siyu Zhang,[1] Min Xu,[1] Tsukasa Kamigaki,[1] Johnny Phong Hoang Do,[1] Wei-Cheng Chang,[1] Sean Jenvay,[1] Kazunari Miyamichi,[2]* Liqun Luo,[2] Yang Dan[1]†

Top-down modulation of sensory processing allows the animal to select inputs most relevant to current tasks. We found that the cingulate (Cg) region of the mouse frontal cortex powerfully influences sensory processing in the primary visual cortex (V1) through long-range projections that activate local γ-aminobutyric acid–ergic (GABAergic) circuits. Optogenetic activation of Cg neurons enhanced V1 neuron responses and improved visual discrimination. Focal activation of Cg axons in V1 caused a response increase at the activation site but a decrease at nearby locations (center-surround modulation). Whereas somatostatin-positive GABAergic interneurons contributed preferentially to surround suppression, vasoactive intestinal peptide-positive interneurons were crucial for center facilitation. Long-range corticocortical projections thus act through local microcircuits to exert spatially specific top-down modulation of sensory processing.

Sensory processing is strongly modulated by the animal's behavioral state. A well-known example is top-down attention, a powerful mechanism for selective processing of behaviorally relevant information and filtering out irrelevant stimuli. In visual cortical areas, many neurons exhibit enhanced responses to attended stimuli (1–4). Several frontal and parietal cortical regions have been implicated as the sources of top-down modulation

signals (*1, 2, 5, 6*), especially the dorsolateral prefrontal cortex and frontal eye field (FEF) (*7–13*). Electrical stimulation of the FEF enhanced V4 neuron responses at the retinotopically corresponding location and suppressed responses at other locations (*11*), resembling the center-surround profile of attentional modulation (*1, 3, 14, 15*). Beyond identifying the signal sources, however, the synaptic circuits mediating top-down modulation are largely unknown. In addition to corticocortical projections, FEF also projects to the thalamus and other subcortical circuits that modulate cortical processing (*16–20*). The role of each pathway has not been clearly delineated. Furthermore, because long-range corticocortical projections are primarily glutamatergic, whether and how they provide center-surround modulation is unknown.

To examine the circuit mechanism of top-down modulation in mouse brain, we first identified neurons in the frontal cortex that directly project to visual cortex by injecting fluorescent latex mi-

[1]Division of Neurobiology, Department of Molecular and Cell Biology, Helen Wills Neuroscience Institute, Howard Hughes Medical Institute, University of California, Berkeley, CA 94720, USA. [2]Department of Biology, Howard Hughes Medical Institute, Stanford University, Stanford, CA 94305, USA.
*Present address: Department of Applied Biological Chemistry, Graduate School of Agricultural and Life Sciences, The University of Tokyo, Tokyo 113-8657, Japan. †Corresponding author. E-mail: ydan@berkeley.edu

crospheres (Retrobeads) into V1. We found numerous retrogradely labeled neurons in the cingulate (Cg) area (Fig. 1, A to C; and fig. S1, A and B). To visualize the axonal projections from Cg excitatory neurons, we injected adeno-associated virus [AAV-CaMKIIα-hChR2(H134R)-EYFP] into Cg. We found enhanced yellow fluorescent protein (EYFP)–labeled axons in both V1 and surrounding visual areas, with the axons in V1 preferentially distributed in layers 1 and 6 (Fig. 1E and fig. S1C). Cg neurons also project to the superior colliculus (Fig. 1, D and E) (*21*).

To test the functional influence of Cg neuron activity on visual processing, we applied laser stimulation to the Cg of the mouse injected with AAV-CaMKIIα-hChR2(H134R)-EYFP (Fig. 2A), which evoked reliable neuronal spiking (Fig. 2B). Cell-attached recordings in V1 of anesthetized mice measured neuronal responses to drifting grating stimuli in both control (laser-off) and Cg activation (laser-on) trials. Cg activation strongly increased V1 neuron firing rate at the preferred orientation but not at nonpreferred orientation (Fig. 2C). This resulted in an approximately multiplicative scaling of the tuning curve (Fig. 2, C and D), similar to the effects of top-down attention (*22*) and FEF stimulation (*11*). Cg activation also increased the slope of V1 neuron response as a function of stimulus contrast (contrast-response function) (fig. S2B). In control mice not injected

with AAV, laser stimulation had no effect (fig. S2, C and D), and the laser-induced response increase was significantly higher in the ChR2 than control mice ($P = 8 \times 10^{-4}$, t test).

To further test the functional influence of Cg activity, we applied optogenetic manipulations in awake mice. Cg activation enhanced V1 responses at a level comparable with that in anesthetized mice (Fig. 2, D and E). Conversely, inactivation of Cg excitatory neurons significantly decreased V1 responses. Stimulation of primate FEF not only enhances visual cortical responses but also improves perceptual performance (*23*). We thus tested the behavioral effect of Cg activation in mice trained to perform a visual discrimination task. Cg activation significantly improved the performance ($P < 0.02$ for each of 5 mice, paired t test) (Fig. 2F). In control mice injected with AAV-CaMKIIα-mCherry, laser had no effect ($P > 0.42$), and the laser-induced improvement was significantly greater for the ChR2 than control mice ($P = 8 \times 10^{-4}$, t test). The laser stimulation used in these experiments evoked no notable eye movement, although stimulation at much higher laser power and frequencies could evoke saccade-like movement.

In principle, Cg neuron activity can influence V1 processing through either the direct projection or indirect pathways via other brain structures. To test whether the direct projection is sufficient for the modulation, we optogenetically

Fig. 1. Cg projects to visual cortex and superior colliculus (SC). (**A**) Schematic of Cg projections. Dashed lines indicate locations of coronal sections shown in this figure: (1), Cg; (2), V1; (3), SC. (**B** to **D**) Retrograde tracing. (B) (Left) Fluorescence image at location (2) showing retrobeads (green) injected into V1. Arrowhead, injection site; red, Nissl staining. (Right) Labeled neurons (dots) at (1), in region outlined by black rectangle (inset). (C) Fluorescence image for red square in (B). Arrowheads indicate labeled neurons. (D) Similar to (B), with retrobeads injected into SC. (**E**) Anterograde tracing from Cg. (Left) Fluorescence image at (1). Arrowhead indicates AAV injection site. (Middle and right) Cg projections to V1 and SC, respectively. SCs/SCm, sensory/motor-related SC.
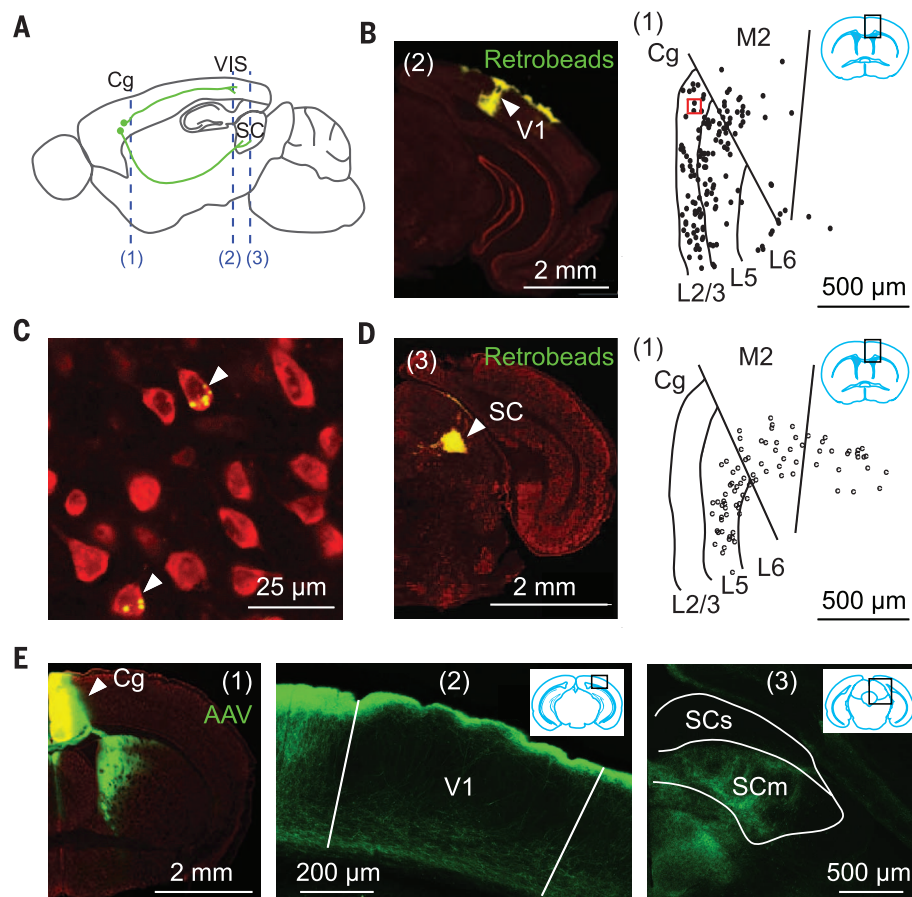
activated Cg axons in V1 of anesthetized mice (Fig. 3A). Laser stimulation in a small area (~200 μm in diameter) encompassing the recorded cell (Fig. 3B) increased both the tuning curve amplitude (Fig. 3, C and D, left) and contrast-response slope (fig. S3). The magnitude of increase was ~70% of that induced through Cg neuron activation (Fig. 2, D and E).

In primates, both top-down attention and FEF stimulation exert center-surround modulation of visual cortical responses (1, 3, 11, 14, 15). We next systematically varied the location of laser stimulation relative to the recorded cell (Fig. 3B). Laser

stimulation at 200 μm significantly decreased the tuning curve amplitude (Fig. 3, C and D, right). The spatial profile of response modulation consisted of a facilitatory center and a suppressive surround (Fig. 3E), reminiscent of the effects of top-down attention (1, 3, 14, 15) and FEF stimulation (11). Activation of Cg axons could antidromically induce spiking of the cell bodies, which may activate axon collaterals to other brain areas. We thus repeated the axon stimulation experiment after blocking spiking in Cg with 2% lidocaine. Similar center-surround modulation was still observed in V1 (fig. S4).

Because the Cg→V1 projections activated in our experiments are glutamatergic, the center-surround modulation is likely to involve V1 local circuits. We therefore made whole-cell recordings in V1 slices. Because the topical laser stimulation used in vivo (Fig. 3, A and B) is likely to activate Cg axons in layer 1 preferentially, in slice experiments we also stimulated layer 1 axons (fig. S5A). We found both excitatory and inhibitory postsynaptic currents (EPSCs and IPSCs) in layer 2/3 pyramidal neurons near the laser stimulation site (fig. S5B). The EPSCs showed short-onset latencies (1.9 ± 0.1 ms, mean ± SEM),
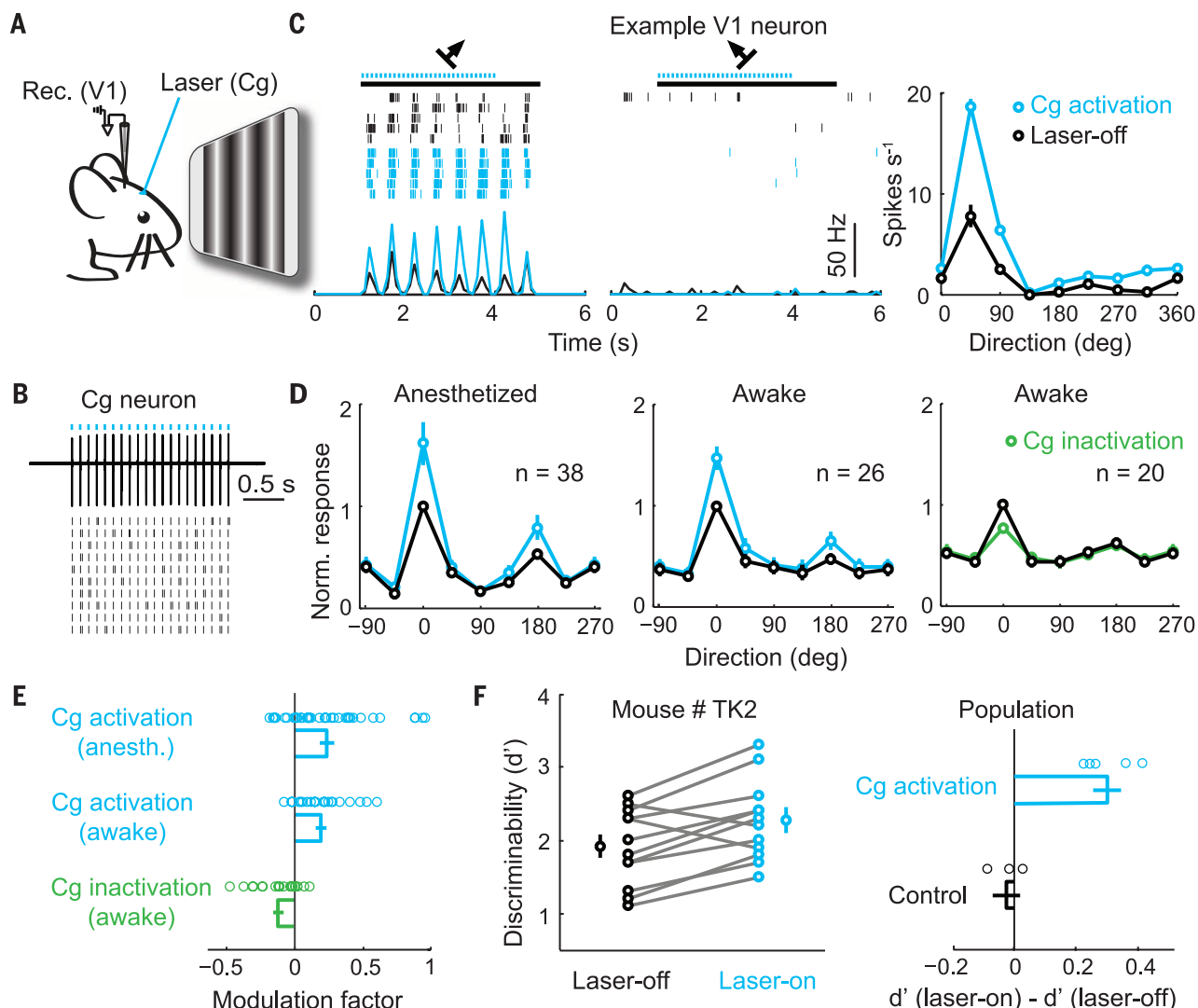

Fig. 2. Cg activation enhances V1 neuron responses and improves visual discrimination. (**A**) Schematic of experiment. (**B**) Cg neuron spiking induced by laser (5 ms/pulse, 10 Hz, blue dots). (Top) Example trace. (Bottom) Raster plot. (**C**) Visual response of a V1 neuron with (blue) or without (black) Cg activation. (Left and middle) Raster plots and PSTHs at preferred and nonpreferred orientations, respectively. Black bar indicates duration of visual stimulation (4 s). (Right) Orientation tuning of this neuron. Error bar, ±SEM. (**D**) Population average of orientation tuning, with each neuron normalized and aligned by its optimal orientation without laser. (Left and middle) Tuning with (blue) and without (black) Cg activation in anesthetized and awake mice, respectively. (Right) Tuning with (green) and without (black) Cg inactivation in awake mice. (**E**) Modulation factors. Cg activation, anesthetized, 0.24 ±

0.05 (mean ± SEM), $P = 10^{-4}$ (t test), n = 38 neurons; awake, 0.19 ± 0.04, $P = 6×10^{-5}$, n = 26 neurons; Cg inactivation: awake, −0.12 ± 0.03, P = 0.003, n = 20 neurons. Each circle represents one neuron. (**F**) Effect of Cg activation on visual discrimination performance. (Left) An example mouse. Each pair of circles represent d′ measured in one day (n = 11 days). Laser-on (blue), 2.27 ± 0.16 (mean ± SEM); laser-off (black), 1.91 ± 0.16, P = 0.005, paired t test. (Right) Population summary of laser-induced change in d′, for Cg activation [mice injected with AAV2/2-CaMKIIα-hChR2(H134R)-EYFP, 0.30 ± 0.04, n = 5 mice] and control (AAV2/2-CaMKIIα-mCherry, −0.02 ± 0.04, n = 3 mice) groups. P_{laser} = 0.002, P_{group} = 0.59, $P_{interaction}$ = 0.0009 [two-way mixed analysis of variance); laser had significant effect only in ChR2 group (P = 0.0006, post-hoc Tukey's test).

suggesting monosynaptic inputs from Cg axons. However, the IPSCs showed significantly longer latencies (6.2 ± 0.4 ms, $P = 5 \times 10^{-14}$, paired t test) and were completely blocked by 6-cyano-7-nitroquinoxaline-2,3-dione (CNQX; 10 μM) (fig. S5C), suggesting disynaptic inhibition. We then measured the excitatory and inhibitory inputs as functions of distance between laser stimulation and the recorded cell (fig. S5, D and E). Although the strength of excitatory input decreased monotonically, the inhibitory input was stronger at 200 than at 0 μm. Such a spatial profile seems well suited for generating surround suppression in vivo (Fig. 3E).

The Cg axon–induced disynaptic inhibition of pyramidal neurons should originate from local γ-aminobutyric acid–ergic (GABAergic) neurons. Parvalbumin-positive (PV+), somatostatin-positive (SOM+), and vasoactive intestinal peptide-positive (VIP+) interneurons are three major nonoverlapping populations of cortical GABAergic neurons (24, 25) and play different roles in visual processing (26–28). To assess the role of each subtype in top-down modulation, we first measured their responses to Cg axon stimulation. Each subtype was identified by breeding loxP-flanked tdTomato reporter mice with PV-, SOM-, or VIP-Cre mice (fig. S6A). Activation of layer 1 Cg axons evoked short-latency (~3 ms) excitatory postsynaptic potentials (EPSPs) in all three interneuron subtypes, even after V1 neuron spiking was blocked with tetrodotoxin (TTX) (fig. S6, B to G) (29). Rabies virus–mediated monosynaptic retrograde tracing (30) confirmed that all three subtypes received direct Cg innervation (fig. S7). The Cg input was stronger in VIP+ than the other neuron types in layer 2/3 (fig. S6), similar to the motor→somatosensory cortex input (31).

We next measured the contribution of each interneuron subtype to disynaptic inhibition of pyramidal neurons using optogenetic inactivation. To express halorhodopsin (Halo) in each subtype, we crossed PV-, SOM-, or VIP-Cre mice with loxP-flanked Halo reporter mice (32). ChR2 was expressed in Cg excitatory neurons by using AAV-CaMKIIα-hChR2(H134R)-EYFP. Inactivation of PV+ neurons (yellow laser, in an area >600 μm in diameter) (Fig. 4A) reduced Cg axon–induced inhibitory inputs at 0, 200, and 400 μm, but the strongest inhibition was still observed at 200 μm (Fig. 4B, left). In contrast, inactivating SOM+ neurons caused the largest reduction of inhibition at 200 μm, so that the strength of inhibition decreased monotonically with distance (middle). Inactivating VIP+ neurons caused an increase in inhibition at 0 μm and no change at other locations (right). Thus, VIP+ neurons caused spatially localized disinhibition, likely by preferentially innervating SOM+ neurons (31, 33–35).

Last, to test the roles of these interneuron subtypes in top-down modulation of visual processing, we optogenetically inactivated them while activating Cg axons in vivo (Fig. 4C). PV+ neuron inactivation caused similar response increases at 0, 200, and 400 μm (Fig. 4, D and E, left). Their inactivation with yellow laser alone without Cg axon stimulation also induced a response increase ($P = 0.01$) (Fig. 4D, yellow circle), suggesting that the effect was partly due to a general reduction of cortical inhibition unrelated to Cg axon stimulation. SOM+ neuron inactivation caused the largest response increase at 200 μm, converting the surround suppression into a slight facilitation (Fig. 4, D and E, middle). The increase at 200 μm was greater than the effect of yellow laser alone ($P = 0.002$), indicating that SOM+ neurons contribute strongly to Cg axon–induced surround suppression. Inactivation of VIP+ neurons, on the other hand, blocked the center facilitation (at 0 μm) without affecting surround suppression (Fig. 4, D and E, right).

We identified a region of mouse frontal cortex that can exert spatially specific top-down modulation of visual processing, which is a hallmark of selective attention. The spatial pattern of Cg projections (Fig. 1 and fig. S1) and its powerful modulation of visual processing indicate functional similarity between mouse Cg and primate
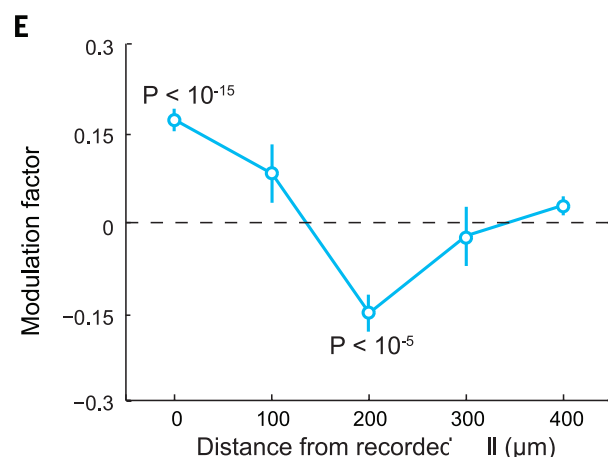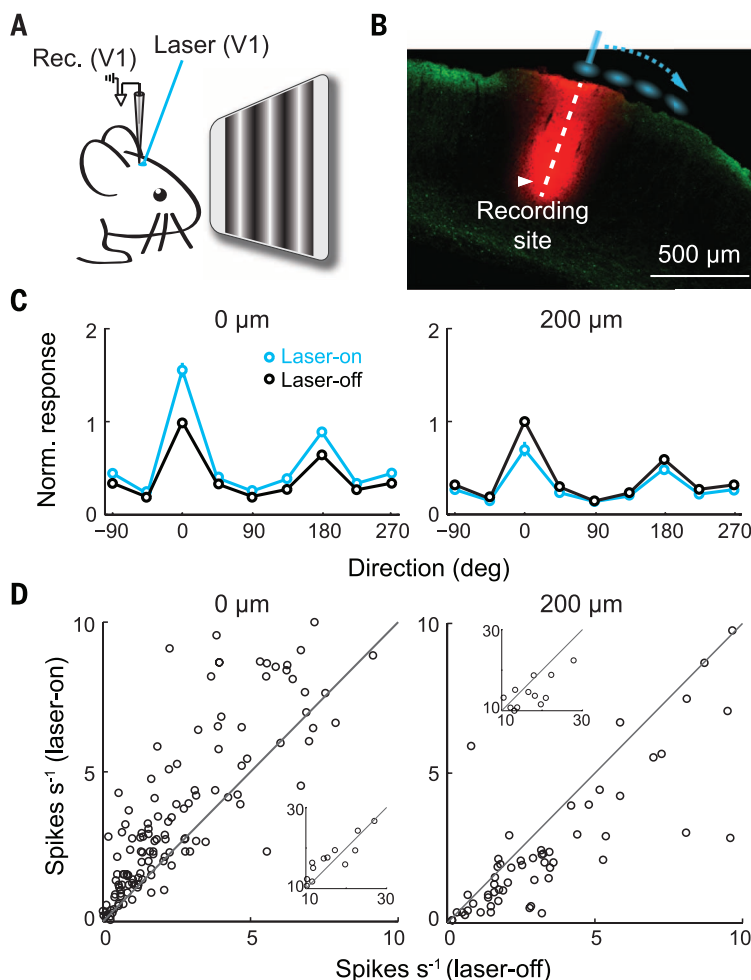

Fig. 3. Focal activation of Cg axons induces center-surround modulation. (**A**) Schematic of experiment. (**B**) Laser stimulation sites (blue) relative to recording site (red, DiI labeling). Green, Cg axons. (**C**) Average tuning curves with (blue) and without (black) laser at 0 μm ($n = 152$) and 200 μm ($n = 78$) from recorded neuron. Error bar, ±SEM. (**D**) Peak firing rate with versus without laser for neurons with peak rates <10 spikes s^{-1}. (Inset) For the neurons with peak rates >10 spikes s^{-1}. Laser-induced significant increase at 0 μm ($P = 2 \times 10^{-10}$, paired t test) and decrease at 200 μm ($P = 3 \times 10^{-5}$). (**E**) Modulation factor versus stimulation location. At 0 μm, 0.17 ± 0.02 (mean ± SEM), $P = 4 \times 10^{-16}$, $n = 152$ neurons; 100 μm, 0.08 ± 0.05, $P = 0.11$, $n = 20$ neurons; 200 μm, −0.15 ± 0.03, $P = 4 \times 10^{-6}$, $n = 78$ neurons; 300 μm, −0.02 ± 0.05, $P = 0.66$, $n = 18$ neurons; 400 μm, 0.04 ± 0.02, $P = 0.06$, $n = 66$ neurons.
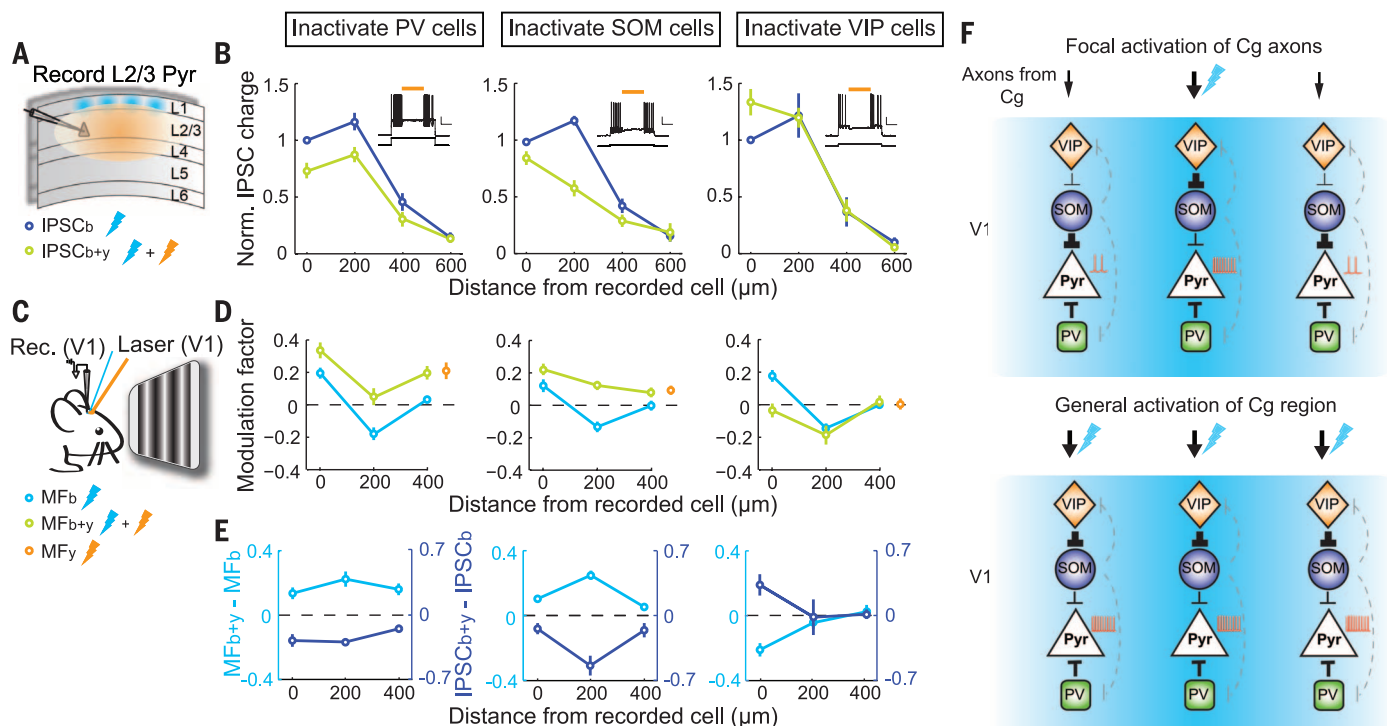
Fig. 4. Contributions of PV+, SOM+, and VIP+ neurons to disynaptic inhibition and top-down modulation. (**A**) Schematic of slice experiment. Thunderbolt denotes laser stimulation. (**B**) (Left) Normalized IPSC charge versus blue light location with (green) or without (blue) PV+ neuron inactivation. Reduction of IPSC was found at 0 μm ($P = 0.004$, $n = 9$ neurons), 200 μm and 400 μm ($P = 0.009$). (Insets) Yellow laser suppressed firing of depolarization-induced PV+ neuron firing (top, membrane potential; yellow bar, yellow laser duration; bottom, current injection; scale bars, 0.5 s, 20 mV/500 pA). (Middle and right) Inactivation of SOM+ ($n = 10$ neurons; 0 μm, $P = 0.04$; 200 μm, $P = 7 \times 10^{-4}$; 400 μm, $P = 0.04$) and VIP+ ($n = 9$ neurons; 0 μm, $P = 0.02$; 200 μm, $P = 0.92$; 400 μm, $P = 0.81$) neurons. Data were from more than three mice in each group. (**C**) Schematic of in vivo experiment. (**D**) Modulation factor versus location of Cg axon stimulation with (green) or without (light blue) PV+, SOM+, or VIP+ neuron inactivation ($n \geq 16$ neurons for each point). PV+ inactivation, 0 μm, $P = 0.005$; 200 μm, $P = 6 \times 10^{-4}$; 400 μm, $P = 5 \times 10^{-4}$. SOM+ inactivation, 0 μm, $P = 2 \times 10^{-4}$; 200 μm, $P = 1 \times 10^{-8}$; 400 μm, $P = 0.02$. VIP + inactivation, 0 μm, $P = 5 \times 10^{-5}$; 200 μm, $P = 0.34$; 400 μm, $P = 0.59$. Yellow circles indicate modulation factor with yellow light only. (**E**) Changes in modulation factor (light blue) and normalized IPSC charge (dark blue) induced with yellow light. (**F**) Diagrams of V1 circuits recruited by Cg projection. (Top) Focal activation. (Bottom) General activation. Thunderbolt denotes site of Cg axon activation. Black lines indicate connections important for top-down modulation; line width represents amplitude of synaptic input. Dashed gray lines indicate other known connections.

FEF (although the FEF projects primarily to higher visual areas rather than V1). In primate visual cortex, top-down attention enhances the firing rates of putative inhibitory interneurons (*14*, *36*). In our study, the three subtypes of interneurons were all innervated by Cg, but they play different roles in top-down modulation. SOM+ neurons strongly inhibit pyramidal neurons in response to Cg input 200 μm away. That they also mediate suppression by visual stimuli outside of the receptive field (*26*) suggests that both bottom-up visual processing and top-down attentional modulation use a common mechanism for surround suppression (*37*). Disinhibition of pyramidal neurons by VIP+ neurons has also been shown in somatosensory (*31*), visual (*33*), auditory (*35*), and medial prefrontal (*35*) cortices, mediating firing rate increases induced by motor activity or reinforcement signals. In the top-down modulation studied here, the disinhibition is highly localized at the site of Cg axon activation (Fig. 4). On the basis of the effect of Halo-mediated inactivation of each cell type, we constructed a simple circuit diagram (Fig. 4F). The Cg→V1 projection provides direct inputs to both GABAergic and pyramidal neurons. In response to focal Cg axon activation, SOM+ and PV+ neurons inhibit pyramidal neurons over a broad cortical area (with SOM+ neurons as a major source of inhibition at 200 μm), whereas VIP+ neurons selectively enhance the responses at 0 μm through localized inhibition of SOM+ neurons (Fig. 4F, left). In contrast, activation of the Cg region induced only facilitation and no suppression (Fig. 2). This may be because given the orientation and small size of Cg (Fig. 1B), topical laser stimulation inevitably activates a large proportion of V1-projecting neurons, causing broad activation of VIP+ neurons that overrides SOM-mediated surround inhibition (Fig. 4F, right). On the other hand, dual retrograde tracing suggests that individual Cg neurons project to restricted regions of V1 (fig. S8), allowing spatially specific top-down modulation.

In addition to PV+, SOM+, and VIP+ neurons, layer 1 GABAergic neurons may also receive Cg innervation, providing both inhibition and disinhibition to pyramidal neurons (*38*, *39*). Besides Cg projection to layer 1, other pathways may also contribute to top-down modulation, including the projection to V1 layer 6 and indirect pathways through other brain areas (*16–19*, *40*). Furthermore, whereas spatial attention involves center-surround modulation in the space domain, feature attention also biases the competition between attended and unattended stimuli (*1*), perhaps via circuit mechanisms similar to those described here but operating in higher visual areas in stimulus feature space (*41*). Enhancing neuronal representation of relevant input and filtering out irrelevant stimuli are two equally important aspects of selective attention. Long-range glutamatergic projections can exert both types of modulation by activating local circuits that contain distinct subtypes of GABAergic interneurons.

REFERENCES AND NOTES

1. R. Desimone, J. Duncan, *Annu. Rev. Neurosci.* **18**, 193–222 (1995).
2. S. Kastner, L. G. Ungerleider, *Annu. Rev. Neurosci.* **23**, 315–341 (2000).
3. J. H. Reynolds, D. J. Heeger, *Neuron* **61**, 168–185 (2009).
4. S. Treue, J. H. Maunsell, *J. Neurosci.* **19**, 7591–7602 (1999).
5. J. W. Bisley, M. E. Goldberg, *Annu. Rev. Neurosci.* **33**, 1–21 (2010).
6. E. K. Miller, J. D. Cohen, *Annu. Rev. Neurosci.* **24**, 167–202 (2001).
7. R. F. Squire, B. Noudoost, R. J. Schafer, T. Moore, *Annu. Rev. Neurosci.* **36**, 451–466 (2013).
8. H. Zhou, R. Desimone, *Neuron* **70**, 1205–1217 (2011).

9. T. J. Buschman, E. K. Miller, *Science* **315**, 1860–1862 (2007).
10. G. G. Gregoriou, S. J. Gotts, H. Zhou, R. Desimone, *Science* **324**, 1207–1210 (2009).
11. T. Moore, K. M. Armstrong, *Nature* **421**, 370–373 (2003).
12. B. Noudoost, T. Moore, *Nature* **474**, 372–375 (2011).
13. L. B. Ekstrom, P. R. Roelfsema, J. T. Arsenault, G. Bonmassar, W. Vanduffel, *Science* **321**, 414–417 (2008).
14. Y. Chen *et al.*, *Nat. Neurosci.* **11**, 974–982 (2008).
15. K. A. Sundberg, J. F. Mitchell, J. H. Reynolds, *Neuron* **61**, 952–963 (2009).
16. K. McAlonan, J. Cavanaugh, R. H. Wurtz, *Nature* **456**, 391–394 (2008).
17. R. Purushothaman, R. Marion, K. Li, V. A. Casagrande, *Nat. Neurosci.* **15**, 905–912 (2012).
18. M. Sarter, M. E. Hasselmo, J. P. Bruno, B. Givens, *Brain Res. Brain Res. Rev.* **48**, 98–111 (2005).
19. Y. B. Saalmann, M. A. Pinsk, L. Wang, X. Li, S. Kastner, *Science* **337**, 753–756 (2012).
20. M. A. Segraves, M. E. Goldberg, *J. Neurophysiol.* **58**, 1387–1419 (1987).
21. The projection to superior colliculus arises only from deep layers (Fig. 1D), similar to that in primate FEF.
22. S. Treue, J. C. Martínez Trujillo, *Nature* **399**, 575–579 (1999).
23. T. Moore, M. Fallah, *J. Neurophysiol.* **91**, 152–162 (2004).
24. X. Xu, K. D. Roby, E. M. Callaway, *J. Comp. Neurol.* **518**, 389–404 (2010).
25. G. Fishell, B. Rudy, *Annu. Rev. Neurosci.* **34**, 535–567 (2011).
26. H. Adesnik, W. Bruns, H. Taniguchi, Z. J. Huang, M. Scanziani, *Nature* **490**, 226–231 (2012).
27. S. H. Lee *et al.*, *Nature* **488**, 379–383 (2012).
28. N. R. Wilson, C. A. Runyan, F. L. Wang, M. Sur, *Nature* **488**, 343–348 (2012).
29. L. Petreanu, T. Mao, S. M. Sternson, K. Svoboda, *Nature* **457**, 1142–1145 (2009).
30. I. R. Wickersham *et al.*, *Neuron* **53**, 639–647 (2007).
31. S. Lee, I. Kruglikov, Z. J. Huang, G. Fishell, B. Rudy, *Nat. Neurosci.* **16**, 1662–1670 (2013).
32. L. Madisen *et al.*, *Nat. Neurosci.* **15**, 793–802 (2012).
33. Y. Fu *et al.*, *Cell* **156**, 1139–1152 (2014).
34. C. K. Pfeffer, M. Xue, M. He, Z. J. Huang, M. Scanziani, *Nat. Neurosci.* **16**, 1068–1076 (2013).
35. H. J. Pi *et al.*, *Nature* **503**, 521–524 (2013).
36. J. F. Mitchell, K. A. Sundberg, J. H. Reynolds, *Neuron* **55**, 131–141 (2007).
37. Based on a magnification factor of 10 μm per degree in mouse V1 (*42*), 200 μm of cortical distance corresponds to 20° of visual angle. A previous study (*26*) showed that for most neurons, the preferred size of visual stimulus was <15° in radius, and stimuli beyond this radius suppressed neuronal responses. This suggests that surround suppression for top-down modulation and bottom-up processing occur on similar spatial scales. The same inhibitory circuits could also contribute to decreased receptive field similarity and signal correlation between V1 neurons over ~200 μm (*42*).
38. J. J. Letzkus *et al.*, *Nature* **480**, 331–335 (2011).
39. X. Jiang, G. Wang, A. J. Lee, R. L. Stornetta, J. J. Zhu, *Nat. Neurosci.* **16**, 210–218 (2013).
40. S. P. Mysore, E. I. Knudsen, *Nat. Neurosci.* **16**, 473–478 (2013).
41. S. Ardid, X. J. Wang, A. Compte, *J. Neurosci.* **27**, 8486–8495 (2007).
42. V. Bonin, M. H. Histed, S. Yurgenson, R. Clay Reid, *J. Neurosci.* **31**, 18506 (2011).

OCEANOGRAPHY

Centennial changes in North Pacific anoxia linked to tropical trade winds

Curtis Deutsch,[1]* William Berelson,[2] Robert Thunell,[3] Thomas Weber,[1] Caitlin Tems,[2] James McManus,[4]† John Crusius,[5] Taka Ito,[6] Timothy Baumgartner,[7] Vicente Ferreira,[7] Jacob Mey,[8,9] Alexander van Geen[8]

Climate warming is expected to reduce oxygen (O_2) supply to the ocean and expand its oxygen minimum zones (OMZs). We reconstructed variations in the extent of North Pacific anoxia since 1850 using a geochemical proxy for denitrification ($\delta^{15}N$) from multiple sediment cores. Increasing $\delta^{15}N$ since ~1990 records an expansion of anoxia, consistent with observed O_2 trends. However, this was preceded by a longer declining $\delta^{15}N$ trend that implies that the anoxic zone was shrinking for most of the 20th century. Both periods can be explained by changes in winds over the tropical Pacific that drive upwelling, biological productivity, and O_2 demand within the OMZ. If equatorial Pacific winds resume their predicted weakening trend, the ocean's largest anoxic zone will contract despite a global O_2 decline.

Below the ocean's surface, the decomposition of sinking detritus creates a layer of low-O_2 water inhospitable to many marine species (*1*). These oxygen minimum zones (OMZs) are predicted to expand with climate warming (*2, 3*), causing a major disruption to ecosystems, especially in areas where OMZ waters impinge on coastal environments already under low-O_2 stress from natural or human causes (*4–6*). This putative expansion stems from two direct consequences of climate change: As the surface ocean warms, its gas solubility and density both decrease, reducing the concentration of O_2 in surface water and the rate at which that water is transported downward against a more stable stratification. The resulting decline in O_2 supply to the ocean interior is generally supported by observed trends toward lower O_2 over the past few decades, over many parts of the world's oceans (*7*), including the strong OMZs in the tropics (*8*).

The climatic response of the OMZ also depends on O_2 demand, although the factors governing those biological rates are less well understood. Earth system model simulations project large future decreases in the sinking flux of organic matter throughout the tropics (*9*), which should reduce O_2 demand in the OMZ, counteracting

the loss of O_2 supply. In the eastern tropical and subtropical Pacific Ocean, the OMZ variability over the last 50 years appears to have been driven primarily by O_2 demand, which is strongly modulated by decadal climate variability (*10, 11*). In light of that variability, the instrumental O_2 record is still sparse and short, making long-term trends in the OMZ difficult to detect or attribute especially in the most intense tropical OMZs in the Pacific and Indian oceans (*8, 12*). The relative strength of future changes in O_2 supply versus demand in the tropical OMZ would be clearer if their long-term response to the climate warming since the industrial revolution were known.

We reconstructed changes in the OMZ of the eastern tropical northern Pacific (ETNP) over the past 150 years using a geochemical proxy for water column anoxia that is recorded in sediments (Fig. 1). At the eastern terminus of the OMZ, where thermocline waters shoal toward the productive surface layer, respiration depletes O_2 and anaerobic bacteria begin reducing nitrate (NO_3^-) to oxidize organic matter (*13*) (Fig. 1). This denitrification process preferentially removes the lighter ^{14}N isotope of N, leaving a residual NO_3^- pool enriched in heavier ^{15}N (*14, 15*). The resulting nitrate with a high isotope ratio, $\delta^{15}N$ [$\delta^{15}N = (^{15}N/^{14}N)/R_{air} - 1) \times 1000$, where R_{air} is the N isotope ratio in air], is upwelled to the surface, where it can be transferred to plankton communities and then, via sinking particles, into sediments (*16, 17*). In regions with complete consumption of upwelled nitrate, the $\delta^{15}N$ of particulate organic nitrogen (PON) accumulating on the sea floor closely resembles that of nitrate in waters at ~100 m (*18*). In the absence of postdepositional alteration, downcore variations in $\delta^{15}N$ provide a history of the integrated rates of denitrification and the size of the OMZ to which it is confined (*19, 20*).

To ensure a representative history of changes in OMZ intensity, we analyzed sediment cores from three sites along the North American margin

[1]School of Oceanography, University of Washington, Seattle, WA, USA. [2]Department of Earth Sciences, University of Southern California, Los Angeles, CA, USA. [3]Department of Earth and Ocean Sciences, University of South Carolina, Columbia, SC, USA. [4]College of Earth, Ocean, and Atmospheric Sciences, Oregon State University, Corvallis, OR, USA. [5]U.S. Geological Survey, University of Washington School of Oceanography, Seattle, WA, USA. [6]School of Earth and Atmospheric Sciences, Georgia Institute of Technology, Atlanta, GA, USA. [7]Departamento de Oceanografía Biológica, Centro de Investigación Científica y de Educación Superior de Ensenada, Baja California, México. [8]Lamont-Doherty Earth Observatory of Columbia University, Palisades, NY, USA. [9]Department of Physical Sciences, Kingsborough Community College, City University of New York, New York, NY, USA.
*Corresponding author. E-mail: cdeutsch@uw.edu †Present address: Department of Geosciences, University of Akron, Akron, OH, USA.

Supplementary Material for

Long-range and local circuits for top-down modulation of visual cortical processing

Siyu Zhang, Min Xu, Tsukasa Kamigaki, Johnny Phong Hoang Do, Wei-Cheng Chang, Sean Jenvay, Kazunari Miyamichi, Liqun Luo, Yang Dan*

*Corresponding author. E-mail: ydan@berkeley.edu

This PDF file includes:

Materials and Methods

Figs. S1 to S8

Full Reference List

Materials and Methods

Animals

All experimental procedures were approved by the Animal Care and Use Committee at the University of California, Berkeley. Experiments were performed on wild-type (C57) and transgenic mice. The transgenic mice used were PV-Cre (Jackson lab stock #008069), SOM-Cre (#013044), VIP-Cre (#010908), CaMKIIα-Cre (#005359), loxP-flanked-tdTomato (#007914), loxP-flanked-Halo-EYFP (#014539) and loxP-flanked-ChR2-EYFP (#012569) mice. To visualize the interneurons, PV-Cre, SOM-Cre or VIP-Cre mice were crossed with loxP-flanked-tdTomato mice. To inactivate the interneurons, PV-Cre, SOM-Cre or VIP-Cre mice were crossed with loxP-flanked-Halo-EYFP mice. To inactivate the Cg excitatory neurons, PV-Cre mice were crossed with loxP-flanked-ChR2-EYFP mice.

Surgery

Adeno-associated viruses (AAVs) were acquired from the UNC Vector Core (AAV2/2-CaMKIIα-hChR2(H134R)-EYFP and AAV2/2-CaMKIIα-mCherry) and Stanford Neuroscience Gene Vector and Virus Core (AAV-DJ-CaMKIIα-hChR2(H134R)-EYFP). For *in vivo* experiments, we used AAV2/2 and AAV-DJ; for *in vitro* experiments, we used AAV-DJ.

Mice (P20-P40) were anesthetized with isoflurane (5% induction and 1.5% maintenance) and placed on a stereotaxic frame. Temperature was kept at 37 °C throughout the procedure using a heating pad. After asepsis, the skin was incised to expose the skull and the overlying connective tissue was removed. A craniotomy (~0.5 mm diameter) was made above the injection site. Viruses or Retrobeads were loaded in a sharp micropipette mounted on a Nanoject II attached to a micromanipulator and then injected at a speed of 60 nL per min. AAV (800 nL) was injected into

the Cg (0.2 mm anterior to bregma and 0.3 mm lateral, at a depth of 0.9 mm). Retrobeads (100-150 nL) were injected into V1 (3.5 mm posterior to bregma and 2.5 mm lateral, at a depth of 0.6 mm) or SC (4.2 mm posterior to bregma and 1 mm lateral, at a depth of 1.8 mm). Histology, *in vivo* recording, and behavioral experiments were performed > 2 weeks after injection. *In vitro* recording was performed 1-2 weeks after injection. For recording and behavioral training in awake mice, a custom-designed headplate was implanted right after the virus injection. Small screws and dental acrylic were used to fix the head plate onto the skull. An optic fiber (200 μm in diameter, N.A. 0.39) with 2.5 mm ferrule stick and a protective cap was then implanted on the surface of the Cg to deliver light.

Histology

Two weeks after the virus or Retrobead injection, the mice were deeply anesthetized with isoflurane and immediately perfused with chilled 0.1 M PBS followed by 4% paraformaldehyde (wt/vol) in PBS. The brain was removed and post-fixed overnight at 4 °C. After fixation, the brain was placed in 30% sucrose (wt/vol) in PBS solution for 1-2 d at 4 °C. After embedding and freezing, the brain was sectioned into 60 μm coronal slices using a cryostat. After rehydration and permeabilization, slices were incubated with the NeuroTrace fluorescent Nissl stains (1:50) for 20 min, then washed with PBS for 2 hrs and mounted with Vectashield. Fluorescence images were taken under a confocal microscope.

Visual stimulation

Visual stimuli were generated with a Graphics card in a PC running custom written software. The mice viewed a gamma-corrected 7" LCD monitor (maximal luminance: 250 cd/m^2) with a refresh rate of 75 Hz. The monitor was placed 10 cm away from the left eye, positioned such that the receptive fields of the recorded neurons were at the center of the monitor. For measuring orientation tuning of V1 neurons, full-field drifting gratings (100% contrast, 2 Hz, 0.04 cycles/°) were presented at 8 directions (separated by 45°) in a pseudorandom sequence. For measuring contrast response, full-field drifting gratings (2 Hz, 0.04 cycles/°) at the preferred orientation of each cell were presented at 11 different contrasts (1%, 10%, 20%, 30%, 40%, 50%, 60%, 70%, 80%, 90% or 100%) in a pseudorandom sequence. Each trial started with 4 s of drift grating, followed by 2 s of gray screen. Laser stimulation lasted for 3 s, starting from the onset of the drifting grating. Baseline firing rates were measured using separate trials with a gray screen (0% contrast). Each block consisted of 18 trials (16 trials at each orientation plus 2 trials at 0% contrast) in orientation tuning measurement, or 24 trials (22 trials at each contrast plus 2 trials at 0% contrast) in contrast response measurement, with interleaved laser-on and laser-off trials. A total of 3-6 blocks were presented in each experiment. For Halo and ChR2 co-activation experiments, blocks with or without yellow laser were interleaved. To measure orientation discrimination in the behavioral experiment, drifting gratings at 0° and 90° (100% contrast, 2 Hz, 0.04 cycles/°, 4 s per trial) were presented to the left eye (see 'Behavior' below).

In vivo recordings and data analysis

Recording experiments were performed >2 weeks after virus injection. For anesthetized experiments, mice were anaesthetized with $5\,\mathrm{mg\,kg^{-1}}$ of chlorprothixene and $0.6\text{-}1.2\,\mathrm{g\,kg^{-1}}$ urethane (IP). A custom headplate was fixed to the skull using glue and dental cement right before recording. Mice were then placed onto a custom platform and their temperature was maintained at $37\,°\mathrm{C}$ using a feedback-controlled heating pad. Two craniotomies (~1.5 mm) were made above the Cg and V1. In a subset of Cg axon stimulation experiments, 2% lidocaine (1-1.5 μL) was injected into the Cg to block antidromic activation of the cell bodies. For awake experiments, mice were habituated to head fixation within the recording setup for several days before recording. Mice were placed in a custom tube and the headplate was fixed on a holder attached to the air table, which allowed them to move the body inside the tube while the head was fixed. On the day of recording, a craniotomy (~1.5 mm diameter) was made above V1 while the animal was under anesthesia (1.5% isoflurane in O_2). The light was delivered through a chronically implanted optic fiber above the Cg.

Cell-attached recordings were made with a Multiclamp 700B amplifier (filtered at 0.5-2 kHz) and sampled at 10 kHz controlled by the Clampex software. Glass pipettes with tip resistance of 4-8 MΩ filled with HEPES buffered ACSF were used. The craniotomy was kept moist with a small bath of ACSF. The reference Ag/AgCl wire was placed in ACSF next to the recording site. For awake experiments, the craniotomy was stabilized with Kwik-Cast after each pipette penetration. Only recordings stable for more than 5 min and with sufficiently high seal resistance (10-100 MΩ) were accepted for analysis. Off-line data analysis was performed using custom software.

To quantify orientation tuning of each neuron, we fitted the firing rate as a function of orientation by the sum of two Gaussian functions with peaks 180° apart:

$$R(\theta) = a_0 + a_1 e^{\frac{-(\theta-\theta_0)^2}{2\sigma^2}} + a_2 e^{\frac{-(\theta-\theta_0+180^o)^2}{2\sigma^2}}$$

where $R(\theta)$ is the response at orientation θ, a_0 is the untuned component of the response, a_1 and a_2 are the amplitudes of the two Gaussians, θ_0 is the preferred orientation, and σ is the standard deviation of the Gaussian function. To quantify the modulation induced by laser stimulation, modulation factor was computed as:

$$MF = (a_{1laser-on} - a_{1laser-off})/(a_{1laser-on} + a_{1laser-off})$$

The fitting error was computed as:

$$E = \sum_{\theta}(R_{measure}(\theta) - R_{fit}(\theta))^2 / \sum_{\theta} R^2_{measure}(\theta)$$

where $R_{measure}(\theta)$ and $R_{fit}(\theta)$ are the measured and fitted responses at θ, respectively. We set a threshold of 0.1 for the fitting error; modulation factor of a cell was included in the analysis only if the fitting error was below the threshold both with and without laser stimulation.

In vivo optical stimulation

Optical activation of ChR2 was induced by blue light. A blue laser (473 nm) was connected to an optic fiber (200 μm in diameter) and controlled by a stimulator. The tip of the optic fiber was placed near the cortical surface, and its position was precisely controlled by a micromanipulator and read out from a DR1000 Digital Readout. To activate the Cg or Cg axons in V1, we used pulse

trains (10 Hz, 5 ms) of laser at a power of 3-5 mW at the fiber tip. To silence Cg by activating

PV+ neurons in PV-ChR2 mice, we used square pulses of laser at the same power.

Optical activation of Halo was induced by yellow light. A yellow laser (593 nm) was

connected to an optic fiber (600 μm in diameter). The yellow light covered the whole area

stimulated by blue light. For SOM-Halo and VIP-Halo experiments, we used yellow light at a

power of 5-8 mW. For PV-Halo experiments, we used a lower power of 1-3 mW to avoid epileptic

discharge. The light (blue and/or yellow) started at the same time as the visual stimulus and lasted

for 3 s.

Behavior

We trained head-fixed mice on a go/no-go visual discrimination task. The detailed method has

been described previously (*27*). Briefly, mice were trained to discriminate between drifting

gratings at 0° and 90° (100% contrast). After training, laser stimulation was applied in 50% of

randomly selected trials, and d' was analyzed separately for trials with and without laser

stimulation. We used 5 AAV2/2-CaMKIIα-hChR2(H134R)-EYFP injected mice for the

experimental group and 3 AAV2/2-CaMKIIα-mCherry injected mice for the control group in

behavioral testing.

Hit and False alarm (FA) rates were quantified as followings:

Hit rate = number of Hits / (number of Hits + number of Misses)

FA rate = number of FAs / (number of FAs + number of CRs)

Based on the Hit and FA rates, orientation discriminability (d') was quantified by:

d' = norminv(Hit rate) – norminv(FA rate)

where norminv is the inverse of the cumulative normal function (*43, 44*). Higher d' values

indicate better performance in visual discrimination.

Slice preparation and recording

Mice were anaesthetized with 5% isoflurane. After decapitation, the brain was dissected rapidly and placed in ice-cold oxygenated HEPES buffered ACSF (in mM: NaCl 92, KCl 2.5, NaH_2PO_4 1.2, $NaHCO_3$ 30, HEPES 20, glucose 25, sodium ascorbate 5, thiourea 2, sodium pyruvate 3, $MgSO_4.7H_2O$ 10, $CaCl_2.2H_2O$ 0.5 and NAC 12, at pH 7.4, adjusted with 10 M NaOH), and coronal sections of primary visual cortex (V1) were made with a vibratome. Slices (350 μm thick) were recovered in oxygenated NMDG-HEPES solution (in mM: NMDG 93, KCl 2.5, NaH_2PO_4 1.2, $NaHCO_3$ 30, HEPES 20, glucose 25, sodium ascorbate 5, thiourea 2, sodium pyruvate 3, $MgSO_4.7H_2O$ 10, $CaCl_2.2H_2O$ 0.5 and NAC 12, at pH 7.4, adjusted with HCl) at 32 °C for 10 min and then maintained in an incubation chamber with oxygenated standard ACSF (in mM: NaCl 125, KCl 3, $CaCl_2$ 2, $MgSO_4$ 2, NaH_2PO_4 1.25, sodium ascorbate 1.3, sodium pyruvate 0.6, $NaHCO_3$ 26, glucose 10 and NAC 10, at pH 7.4, adjusted by 10 M NaOH) at 25 °C for 1-4 hr before recording (*45*).

Whole-cell recordings were made at 30 °C in oxygenated solution (in mM: NaCl 125, KCl 4, $CaCl_2$ 2, $MgSO_4$ 1, NaH_2PO_4 1.25, sodium ascorbate 1.3, sodium pyruvate 0.6, $NaHCO_3$ 26 and glucose 10, at pH 7.4). EPSPs were recorded using a potassium based internal solution (in mM: K-gluconate 135, KCl 5, HEPES 10, EGTA 0.3, MgATP 4, Na_2GTP 0.3, and Na_2-phosphocreatine 10, at pH 7.3, adjusted with KOH, 290-300 mOsm). EPSCs and IPSCs were recorded using a cesium-based internal solution (in mM: $CsMeSO_4$ 125, CsCl 2, HEPES 10, EGTA 0.5, MgATP 4, Na_2GTP 0.3, Na_2-phosphocreatine 10, TEACl 5, QX-314 3.5, at pH 7.3, adjusted with CsOH, 290-300 mOsm) and isolated by clamping the membrane potential of the recorded neuron at the reversal potential of inhibitory and excitatory synaptic currents, respectively. For measuring the monosynaptic inputs from Cg axons to V1 neurons (fig. S5), TTX (1 μM) and 4-aminopyridine

(100µM) were bath applied to block action potentials and permit direct depolarization of axon terminals by ChR2 activation with 5-ms pulses of blue light (*29*). The resistance of patch pipette was 3-5 MΩ. The cells were excluded if the series resistance exceeded 40 MΩ or varied by more than 20% during the recording period. Data were recorded with an amplifier filtered at 2 kHz and digitized at 10 kHz. Recordings were analyzed using custom software.

Optical stimulation in slices

To activate ChR2, we used mercury arc lamp gated by an electromagnetic shutter coupled to the epifluorescence light path and bandpass filtered at 419-465 nm, which minimized co-activation of Halo. Pulse trains of blue light (10 Hz, 5 ms) were delivered through a 40× 0.8 NA water immersion lens at a power of 1-2 mW. The size of the light spot was controlled by a calibrated aperture on a microscope. To activate Halo, a 600 µm optic fiber was coupled to a yellow laser (593 nm) and controlled by a stimulator. The optic fiber was mounted on a micromanipulator and placed < 1 mm from the recorded area under the 40× objective. We used square pulse of yellow light at a power of 5 mW.

Rabies-virus-based retrograde monosynaptic tracing

Glycoprotein-deleted (ΔG) and EnvA-pseudotyped rabies virus (RV-ΔG-tdTomato+EnvA) was used for retrograde monosynaptic tracing from different types of V1 neurons (*46, 47*). TVA receptor and rabies glycoprotein, which are required for virus infection and trans-synaptic spread, respectively, were expressed in Cre-positive neurons by co-injection of AAV2/2-EF1α-DIO-TVA-EGFP and AAV2/2-EF1α-DIO-Glycoprotein (400 nL) into V1 of CaMKIIα-Cre, PV-Cre, SOM-Cre and VIP-Cre mice. RV-ΔG-tdTomato+EnvA (400 nL) was injected two weeks after AAV injection. The histology experiments were performed 7 days after rabies virus injection.

AAV preparation followed previously reported protocol (*48*). To construct AAV-EF1α-DIO-TVA-EGFP and AAV-EF1α-DIO-Glycoprotein, TVA and EGFP linked by the 2A 'self-cleaving' peptides or rabies glycoprotein was cloned into pAAV-MCS in an antisense direction flanked by a pair of canonical loxP sites and a pair of lox2272 sites. AAV particles (AAV2/2) were produced by co-transfection of packaging plasmids into HEK293T cells, and cell lysates were fractionated by iodixanol gradient ultracentrifugation. Viral particles were further purified from the crude fraction by heparin affinity column, desalted and concentrated with centrifugal filter (100K). The genomic titer of AAV2/2-EF1α-DIO-TVA-EGFP (4.4×10^{13} gc/mL) and AAV2/2-EF1α-DIO-Glycoprotein (2.2×10^{12} gc/mL) was determined by quantitative PCR. TVA and rabies glycoprotein were subcloned from the AAV-TRE-HTG plasmid from L. Luo (*49*).

RV-ΔG-tdTomato was amplified in B7GG cells and pseudotyped using BHK-EnvA cells in a manner similar to that previously described by (*50*). EnvA pseudotyped rabies virus was titered (1.2×10^{8} IU/mL) using HEK293-TVA cells. RV-ΔG-tdTomato was a gift from B. Lim. B7GG cells, BHK-EnvA cells and HEK293-TVA cells were gifts from E. Callaway.

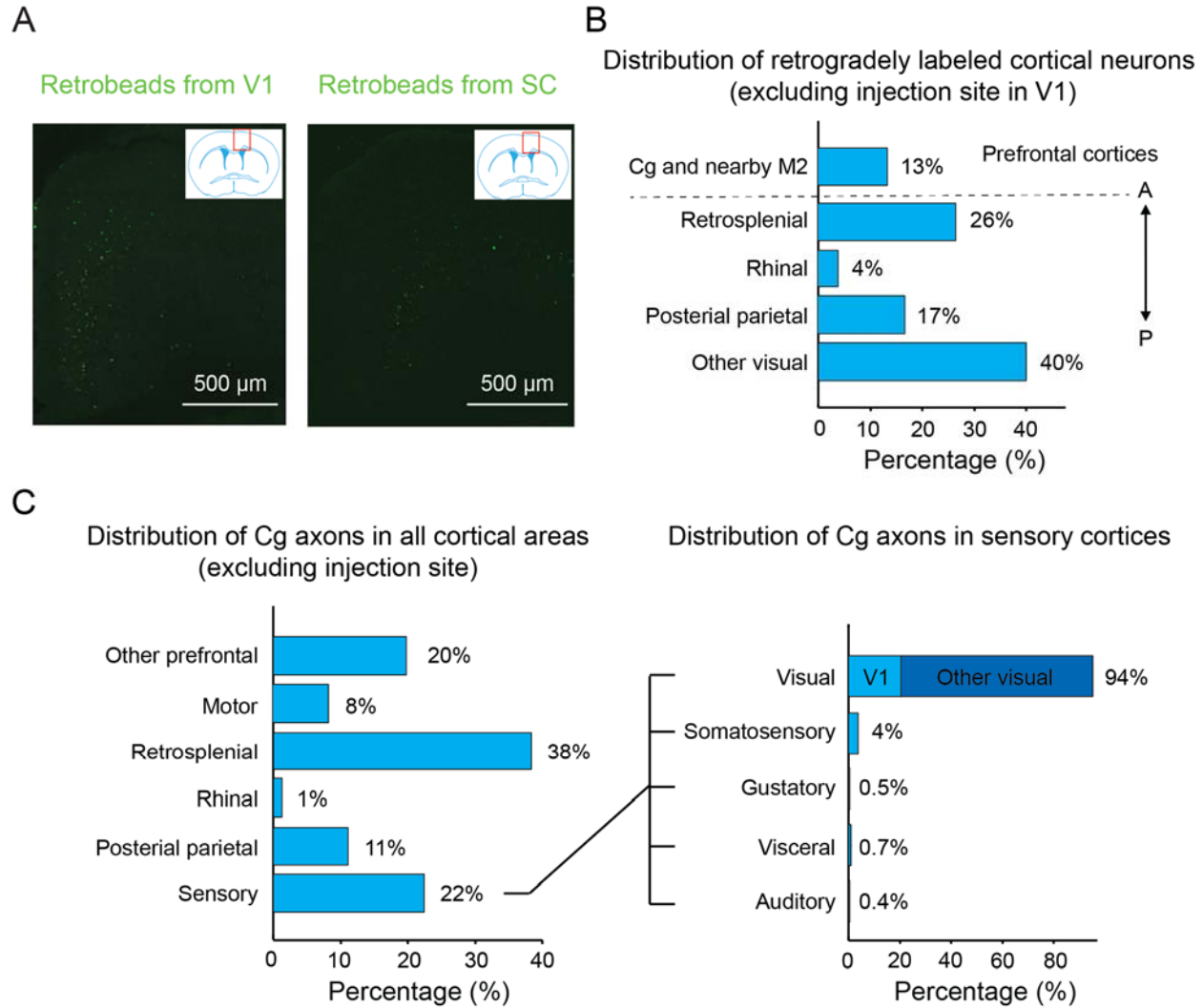**Supplementary Figures and Legends**

Fig. S1. Retrograde tracing from V1 and SC and anterograde tracing from Cg. (A) Fluorescence images of Retrobeads-labeled neurons in Cg, corresponding to the line drawings in Fig. 1, B and D. **(B)** Distribution of neurons retrogradely labeled from V1 in different cortical areas. In the frontal area only Cg and the immediately adjacent M2 were labeled. **(C)** Distribution of Cg axons in different cortical areas, based on data from Allen Mouse Brain Connectivity Atlas, http://connectivity.brain-map.org/ (*51*). Among sensory cortices, visual areas receive 94% of the Cg projections.
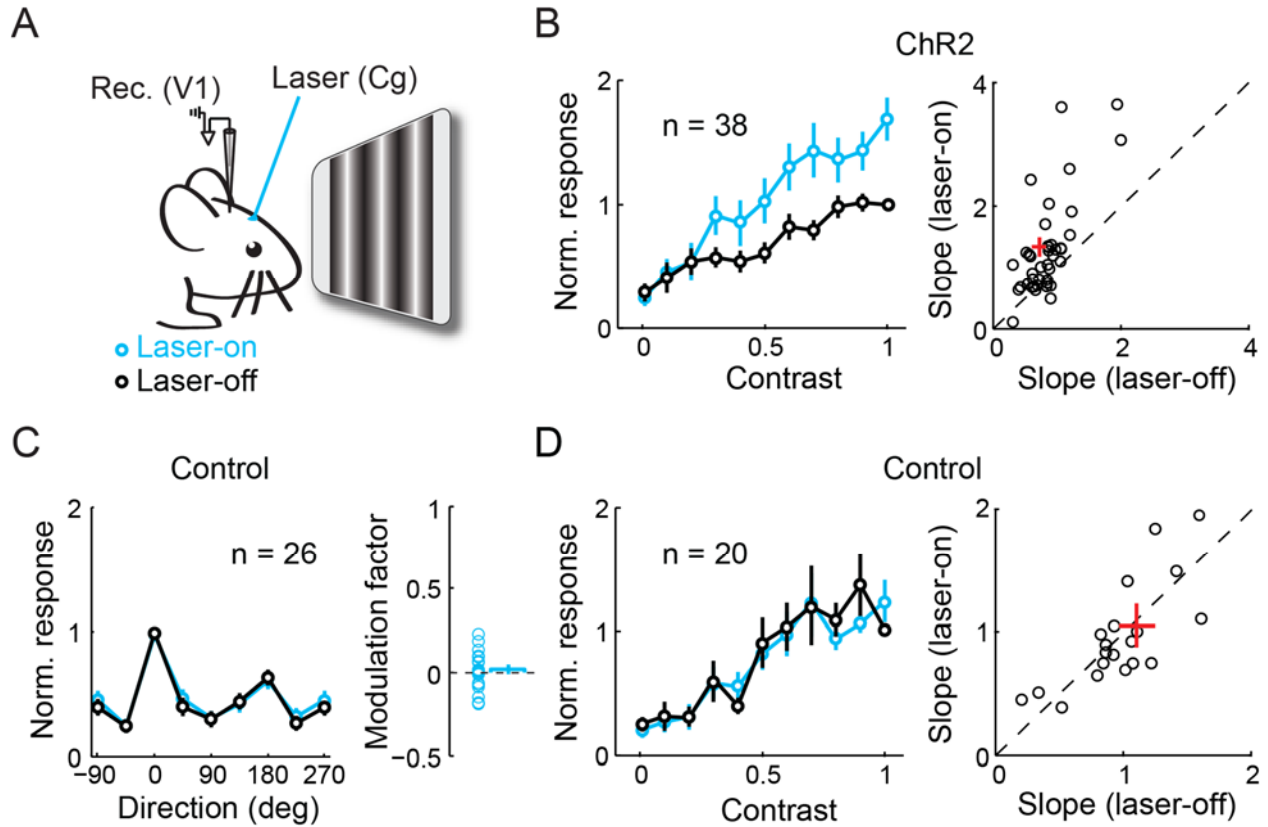
Fig. S2. Effects of laser stimulation on contrast-response function in ChR2-expressing and control mice. **(A)** Schematic of experimental setup. **(B)** Contrast-response function (measured at the preferred orientation of each cell) in ChR2 mice. Left, population contrast-response function with (blue) or without (black) laser stimulation. The functions of each cell were normalized by its firing rate at 100% contrast without laser stimulation. Right, Slope of contrast-response function of each neuron in laser-on vs. laser-off trials ($P < 10^{-4}$, paired t-test). Each circle represents one cell. Red cross, mean ± SEM. **(C)** Left, population orientation tuning curves with (blue) or without (black) laser stimulation in control mice (not injected with AAV). Right, Modulation factors in control mice (mean ± SEM., -0.014 ± 0.005, $P = 0.6$, t-test). Each circle represents one neuron. **(D)** Similar to (B), for control mice ($P = 0.4$, paired t-test). Error bars, mean ± SEM.
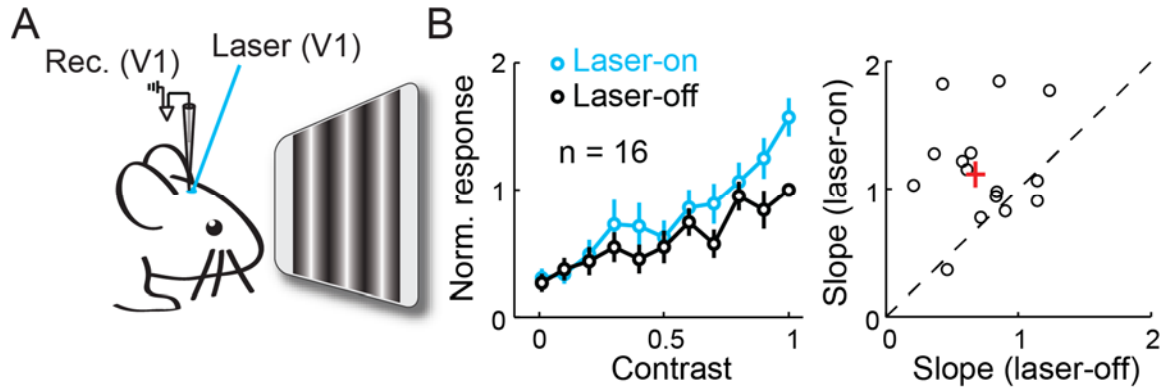
Fig. S3. Activation of Cg axons in V1 increases the slope of contrast-response function at the site of activation. **(A)** Schematic of experimental setup. **(B)** Left, population contrast-response function with (blue) or without (black) laser stimulation. Error bars, mean ± SEM. Right, Slope of contrast-response function of each neuron in laser-on vs. laser-off trials ($P = 0.002$, paired *t*-test). Red cross, mean ± SEM.
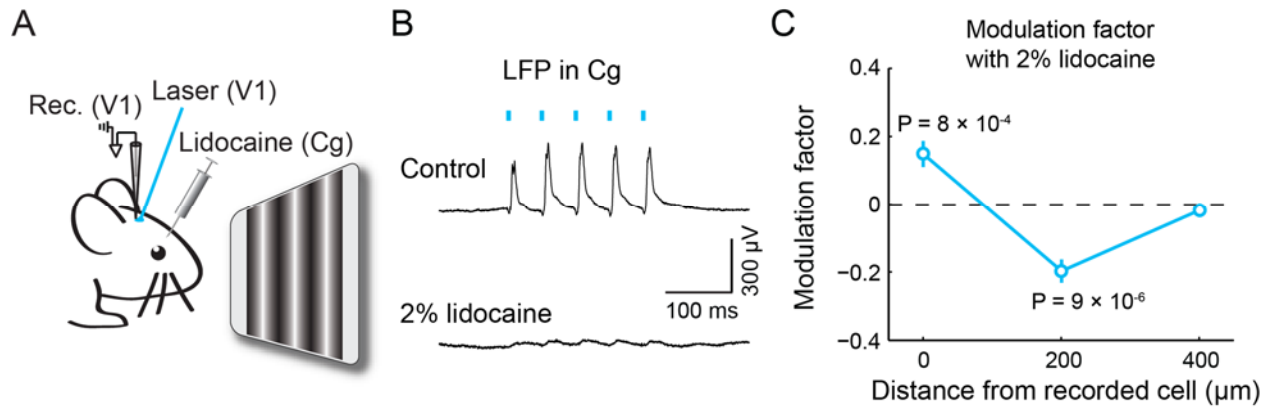
Fig. S4. Center-surround modulation of visual cortical responses induced by Cg axon stimulation after blocking antidromic spiking of Cg neurons. (**A**) Schematic of experimental setup. (**B**) Lidocaine injection into Cg abolished local field potential (LFP) responses recorded in Cg evoked by light stimulation in V1. (**C**) Modulation factor vs. stimulation location in V1 in the presence of lidocaine in Cg. At 0 μm, 0.15 ± 0.04 (mean ± SEM), $P = 8 \times 10^{-4}$, $n = 20$; 200 μm, -0.19 ± 0.03, $P = 9 \times 10^{-6}$, $n = 24$; 400 μm, -0.01 ± 0.02, $P = 0.53$, $n = 19$.
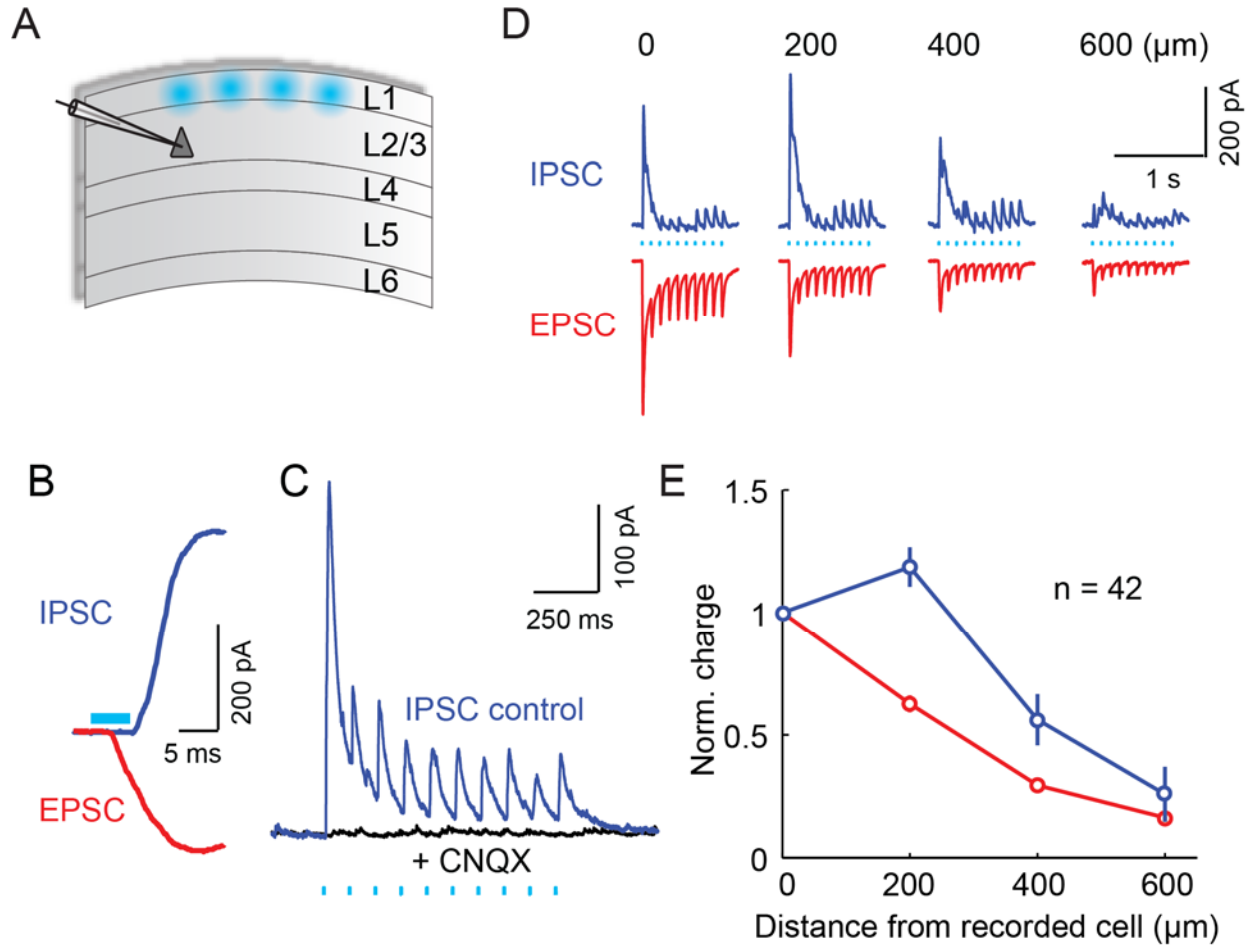
Fig. S5. Disynaptic inhibition of pyramidal neurons evoked by Cg axon stimulation. (A) Schematic of slice experiment, with whole-cell recording from layer 2/3 pyramidal neurons and focal activation of Cg axons in layer 1. **(B)** The enlarged initial part of light-evoked EPSC (red) and IPSC (blue) in an example L2/3 pyramidal neuron. Cyan bar, duration of light stimulation (5 ms). **(C)** IPSC with (black) or without (blue) AMPA type glutamate receptor antagonist (CNQX, 10 µM). Cyan dots, 5-ms light stimulation (10 Hz). **(D)** EPSCs and IPSCs in a layer 2/3 pyramidal neuron at different stimulus locations. **(E)** Normalized excitatory (red) and inhibitory (blue) input strengths (measured by total charge) vs. stimulus location for all recorded L2/3 pyramidal neurons (*n* = 42). Each input was normalized by its strength at 0 µm. At 200 µm, excitatory input was significantly weaker than that at 0 µm ($P = 3\times10^{-15}$, *t*-test), inhibitory input was significantly stronger ($P = 0.01$, *t*-test).
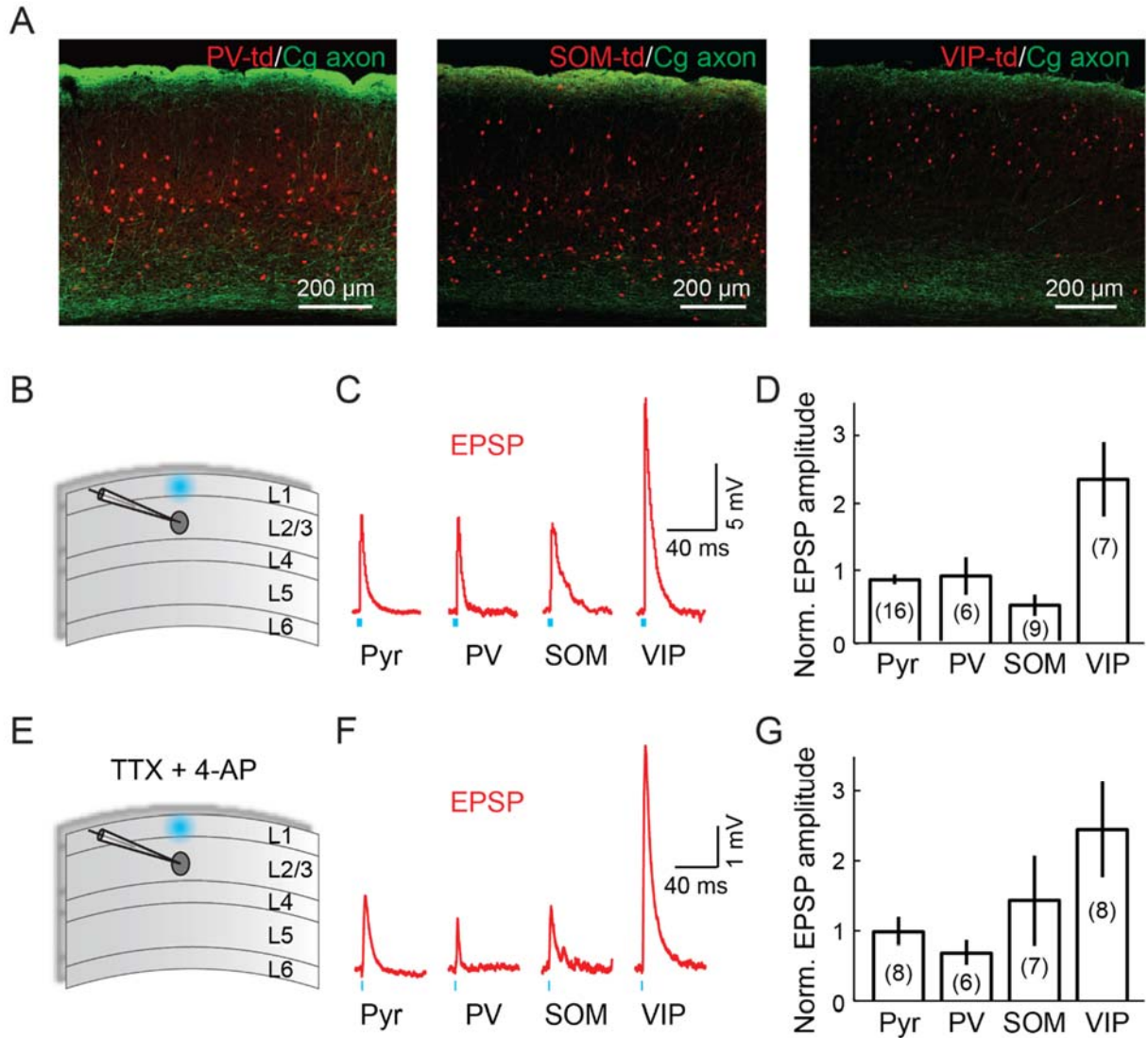
Fig. S6. Subtypes of V1 neurons receiving direct excitatory inputs from Cg. (**A**) Cg axons (green) in V1 of PV-tdTomato (left), SOM-tdTomato (middle) and VIP-tdTomato (right) mice. Red, PV+, SOM+ or VIP+ neurons expressing tdTomato. Scale bar, 200 µm. (**B**) Schematic of experimental setup for slice recording in V1. (**C**) Example blue light-evoked EPSPs recorded from pyramidal (Pyr), PV+, SOM+ and VIP+ neurons. (**D**) Normalized EPSP amplitudes in different cell types (normalized by EPSP amplitude from the most superficial L2/3 Pyr neuron recorded on the same day). EPSP amplitude in VIP+ neurons was larger than those in any other group ($P <$ 0.03, *t*-test). (**E-G**) Similar to (**B-D**), but in the presence of TTX (1 µM) and 4-AP (100 µM). In this experiment, TTX (which blocks sodium channels and therefore action potentials of V1 neurons) was used to eliminate polysynaptic responses evoked by Cg axon stimulation. However, since TTX also greatly attenuates the monosynaptic responses, 4-AP (which blocks the potassium channels and thus allows direct depolarization of axon terminals by ChR2 activation) was used to boost the monosynaptic inputs from Cg axons (*29*). Blue dot, 5-ms blue light pulse.
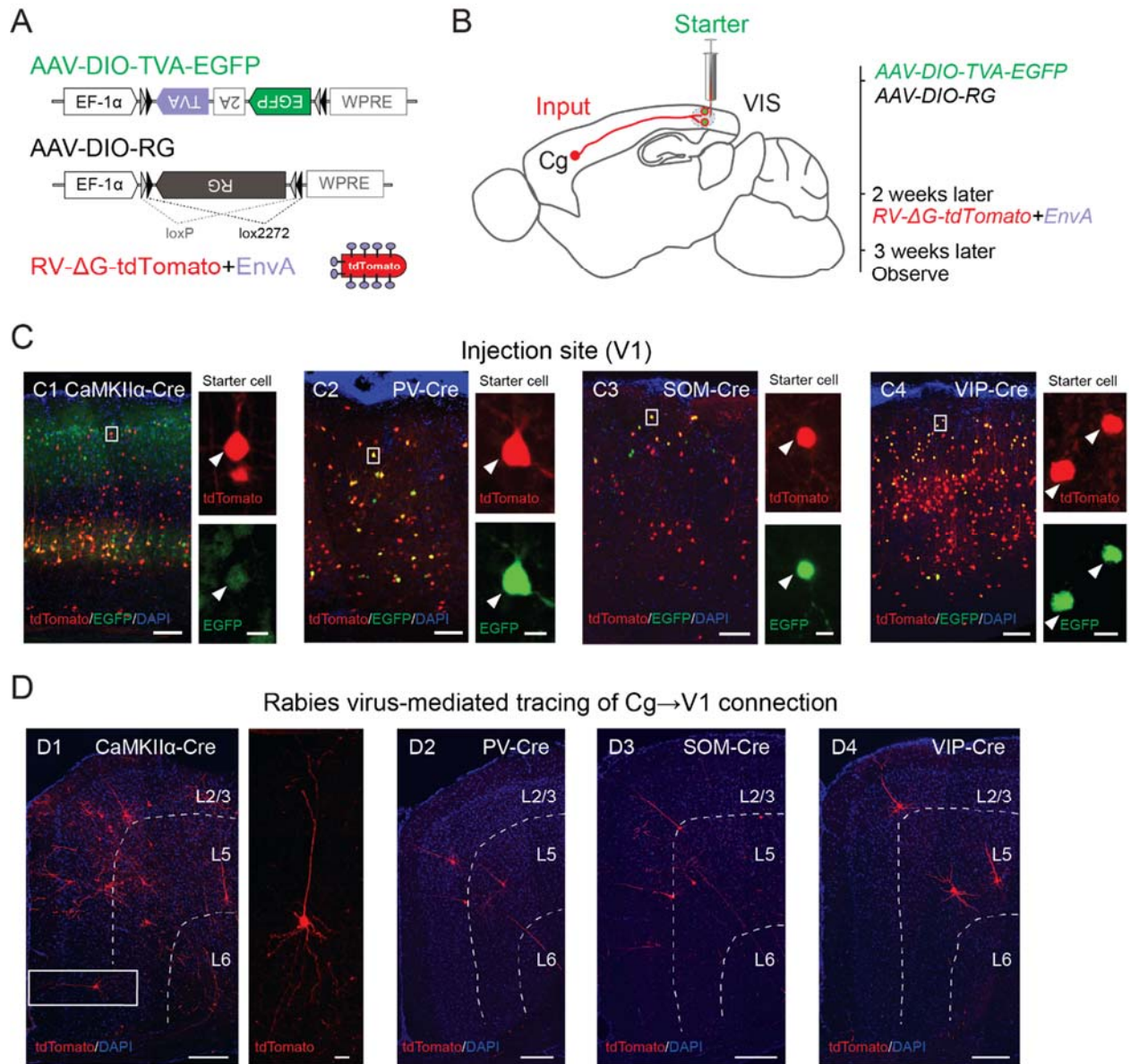
Fig. S7. Monosynaptic innervation of different cell types in V1 by Cg neurons detected by rabies virus-based circuit tracing. (A) Schematics for the AAV vectors (used for cell type-specific expression of TVA receptor and rabies glycoprotein) and rabies virus. **(B)** Schematic of experimental procedure. **(C)** Injection sites in V1 of CaMKIIα-, PV-, SOM- and VIP-Cre mice. (C1) Left, starter cells (yellow) and AAV-transduced cells that did not receive RV (green) were found in V1 of a CaMKIIα-Cre mouse. Scale bar, 100 μm. Right, fluorescence image for the small white square in the left panel. Arrowheads point to a starter neuron. Scale bar, 10 μm. (C2 to C4) Similar to (C1), but with AAV and rabies virus injected into V1 of PV-, SOM- or VIP-Cre mice. **(D)** Transsynaptically labeled tdTomato+ neurons (red) in Cg. (D1) Left, Cg neurons innervating CaMKIIα+ excitatory neurons in V1. Scale bar, 200 μm. Right, enlarged image (rotated 90°) for the white rectangle in the left panel. Scale bar, 20μm. (D2 to D4) Similar to (D1), but for Cg neurons innervating PV+, SOM+ and VIP+ interneurons in V1 respectively. Dashed lines, estimated borders between layers.
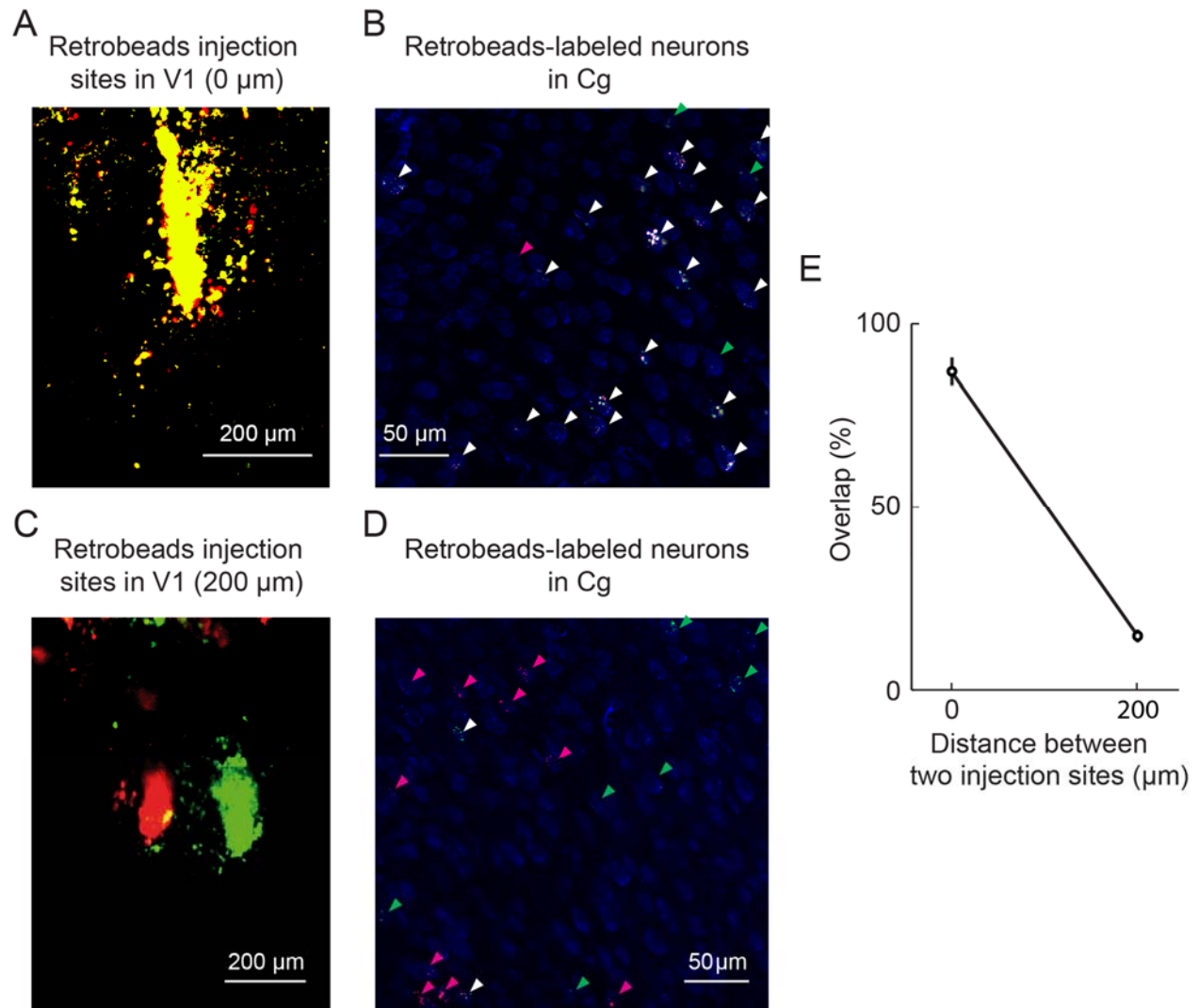
Fig. S8. Dual retrograde tracing of Cg neurons projecting to different V1 locations. (A) Sites of injection of red and green Retrobeads (at the same location, 0 μm) in V1 of a representative experiment. **(B)** Images of Retrobeads-labeled Cg neurons. Red/green arrowheads, neurons labeled with red/green beads; white arrowheads, double labeled neurons. **(C and D)** Similar to **(A and B)**, but the red and green beads were injected in V1 ~200 μm apart from each other. **(E)** Quantification of the overlap between Cg neurons projecting to the two V1 locations (0 μm, $n = 3$ mice; 200 μm, $n = 3$ mice). Shown are mean ± SEM of the percentages of double labeled cells across mice. The low degree of overlap between Cg neurons projecting to the two locations 200 μm apart was not due to a low efficiency of retrograde labeling, since injection of red and green beads at the same V1 location revealed a high degree of overlap.

References and Notes

1. R. Desimone, J. Duncan, Neural mechanisms of selective visual attention. *Annu. Rev. Neurosci.* **18**, 193–222 (1995). Medline doi:10.1146/annurev.ne.18.030195.001205

2. S. Kastner, L. G. Ungerleider, Mechanisms of visual attention in the human cortex. *Annu. Rev. Neurosci.* **23**, 315–341 (2000). Medline doi:10.1146/annurev.neuro.23.1.315

3. J. H. Reynolds, D. J. Heeger, The normalization model of attention. *Neuron* **61**, 168–185 (2009). Medline doi:10.1016/j.neuron.2009.01.002

4. S. Treue, J. H. Maunsell, Effects of attention on the processing of motion in macaque middle temporal and medial superior temporal visual cortical areas. *J. Neurosci.* **19**, 7591–7602 (1999). Medline

5. J. W. Bisley, M. E. Goldberg, Attention, intention, and priority in the parietal lobe. *Annu. Rev. Neurosci.* **33**, 1–21 (2010). Medline doi:10.1146/annurev-neuro-060909-152823

6. E. K. Miller, J. D. Cohen, An integrative theory of prefrontal cortex function. *Annu. Rev. Neurosci.* **24**, 167–202 (2001). Medline doi:10.1146/annurev.neuro.24.1.167

7. R. F. Squire, B. Noudoost, R. J. Schafer, T. Moore, Prefrontal contributions to visual selective attention. *Annu. Rev. Neurosci.* **36**, 451–466 (2013). Medline doi:10.1146/annurev-neuro-062111-150439

8. H. Zhou, R. Desimone, Feature-based attention in the frontal eye field and area V4 during visual search. *Neuron* **70**, 1205–1217 (2011). Medline doi:10.1016/j.neuron.2011.04.032

9. T. J. Buschman, E. K. Miller, Top-down versus bottom-up control of attention in the prefrontal and posterior parietal cortices. *Science* **315**, 1860–1862 (2007). Medline doi:10.1126/science.1138071

10. G. G. Gregoriou, S. J. Gotts, H. Zhou, R. Desimone, High-frequency, long-range coupling between prefrontal and visual cortex during attention. *Science* **324**, 1207–1210 (2009). Medline doi:10.1126/science.1171402

11. T. Moore, K. M. Armstrong, Selective gating of visual signals by microstimulation of frontal cortex. *Nature* **421**, 370–373 (2003). Medline doi:10.1038/nature01341

12. B. Noudoost, T. Moore, Control of visual cortical signals by prefrontal dopamine. *Nature* **474**, 372–375 (2011). Medline doi:10.1038/nature09995

13. L. B. Ekstrom, P. R. Roelfsema, J. T. Arsenault, G. Bonmassar, W. Vanduffel, Bottom-up dependent gating of frontal signals in early visual cortex. *Science* **321**, 414–417 (2008). Medline doi:10.1126/science.1153276

14. Y. Chen, S. Martinez-Conde, S. L. Macknik, Y. Bereshpolova, H. A. Swadlow, J. M. Alonso, Task difficulty modulates the activity of specific neuronal populations in primary visual cortex. *Nat. Neurosci.* **11**, 974–982 (2008). Medline doi:10.1038/nn.2147

15. K. A. Sundberg, J. F. Mitchell, J. H. Reynolds, Spatial attention modulates center-surround interactions in macaque visual area v4. *Neuron* **61**, 952–963 (2009). Medline doi:10.1016/j.neuron.2009.02.023

16. K. McAlonan, J. Cavanaugh, R. H. Wurtz, Guarding the gateway to cortex with attention in visual thalamus. *Nature* **456**, 391–394 (2008). Medline doi:10.1038/nature07382

17. G. Purushothaman, R. Marion, K. Li, V. A. Casagrande, Gating and control of primary visual cortex by pulvinar. *Nat. Neurosci.* **15**, 905–912 (2012). Medline doi:10.1038/nn.3106

18. M. Sarter, M. E. Hasselmo, J. P. Bruno, B. Givens, Unraveling the attentional functions of cortical cholinergic inputs: Interactions between signal-driven and cognitive modulation of signal detection. *Brain Res. Brain Res. Rev.* **48**, 98–111 (2005). Medline doi:10.1016/j.brainresrev.2004.08.006

19. Y. B. Saalmann, M. A. Pinsk, L. Wang, X. Li, S. Kastner, The pulvinar regulates information transmission between cortical areas based on attention demands. *Science* **337**, 753–756 (2012). Medline doi:10.1126/science.1223082

20. M. A. Segraves, M. E. Goldberg, Functional properties of corticotectal neurons in the monkey's frontal eye field. *J. Neurophysiol.* **58**, 1387–1419 (1987). Medline

21. The projection to superior colliculus arises only from deep layers (Fig. 1D), similar to that in primate FEF.

22. S. Treue, J. C. Martínez Trujillo, Feature-based attention influences motion processing gain in macaque visual cortex. *Nature* **399**, 575–579 (1999). Medline doi:10.1038/21176

23. T. Moore, M. Fallah, Microstimulation of the frontal eye field and its effects on covert spatial attention. *J. Neurophysiol.* **91**, 152–162 (2004). Medline doi:10.1152/jn.00741.2002

24. X. Xu, K. D. Roby, E. M. Callaway, Immunochemical characterization of inhibitory mouse cortical neurons: Three chemically distinct classes of inhibitory cells. *J. Comp. Neurol.* **518**, 389–404 (2010). Medline doi:10.1002/cne.22229

25. G. Fishell, B. Rudy, Mechanisms of inhibition within the telencephalon: "Where the wild things are". *Annu. Rev. Neurosci.* **34**, 535–567 (2011). Medline doi:10.1146/annurev-neuro-061010-113717

26. H. Adesnik, W. Bruns, H. Taniguchi, Z. J. Huang, M. Scanziani, A neural circuit for spatial summation in visual cortex. *Nature* **490**, 226–231 (2012). Medline doi:10.1038/nature11526

27. S. H. Lee, A. C. Kwan, S. Zhang, V. Phoumthipphavong, J. G. Flannery, S. C. Masmanidis, H. Taniguchi, Z. J. Huang, F. Zhang, E. S. Boyden, K. Deisseroth, Y. Dan, Activation of specific interneurons improves V1 feature selectivity and visual perception. *Nature* **488**, 379–383 (2012). Medline doi:10.1038/nature11312

28. N. R. Wilson, C. A. Runyan, F. L. Wang, M. Sur, Division and subtraction by distinct cortical inhibitory networks in vivo. *Nature* **488**, 343–348 (2012). Medline doi:10.1038/nature11347

29. L. Petreanu, T. Mao, S. M. Sternson, K. Svoboda, The subcellular organization of neocortical excitatory connections. *Nature* **457**, 1142–1145 (2009). Medline doi:10.1038/nature07709

30. I. R. Wickersham, D. C. Lyon, R. J. Barnard, T. Mori, S. Finke, K. K. Conzelmann, J. A. Young, E. M. Callaway, Monosynaptic restriction of transsynaptic tracing from single,

genetically targeted neurons. *Neuron* **53**, 639–647 (2007). [Medline](#) [doi:10.1016/j.neuron.2007.01.033](#)

31. S. Lee, I. Kruglikov, Z. J. Huang, G. Fishell, B. Rudy, A disinhibitory circuit mediates motor integration in the somatosensory cortex. *Nat. Neurosci.* **16**, 1662–1670 (2013). [Medline](#) [doi:10.1038/nn.3544](#)

32. L. Madisen, T. Mao, H. Koch, J. M. Zhuo, A. Berenyi, S. Fujisawa, Y. W. Hsu, A. J. Garcia 3rd, X. Gu, S. Zanella, J. Kidney, H. Gu, Y. Mao, B. M. Hooks, E. S. Boyden, G. Buzsáki, J. M. Ramirez, A. R. Jones, K. Svoboda, X. Han, E. E. Turner, H. Zeng, A toolbox of Cre-dependent optogenetic transgenic mice for light-induced activation and silencing. *Nat. Neurosci.* **15**, 793–802 (2012). [Medline](#) [doi:10.1038/nn.3078](#)

33. Y. Fu, J. M. Tucciarone, J. S. Espinosa, N. Sheng, D. P. Darcy, R. A. Nicoll, Z. J. Huang, M. P. Stryker, A cortical circuit for gain control by behavioral state. *Cell* **156**, 1139–1152 (2014). [Medline](#) [doi:10.1016/j.cell.2014.01.050](#)

34. C. K. Pfeffer, M. Xue, M. He, Z. J. Huang, M. Scanziani, Inhibition of inhibition in visual cortex: The logic of connections between molecularly distinct interneurons. *Nat. Neurosci.* **16**, 1068–1076 (2013). [Medline](#) [doi:10.1038/nn.3446](#)

35. H. J. Pi, B. Hangya, D. Kvitsiani, J. I. Sanders, Z. J. Huang, A. Kepecs, Cortical interneurons that specialize in disinhibitory control. *Nature* **503**, 521–524 (2013). [Medline](#) [doi:10.1038/nature12676](#)

36. J. F. Mitchell, K. A. Sundberg, J. H. Reynolds, Differential attention-dependent response modulation across cell classes in macaque visual area V4. *Neuron* **55**, 131–141 (2007). [Medline](#) [doi:10.1016/j.neuron.2007.06.018](#)

37. Based on a magnification factor of 10 μm per degree in mouse V1 (*42*), 200 μm of cortical distance corresponds to 20° of visual angle. A previous study (*26*) showed that for most neurons, the preferred size of visual stimulus was <15° in radius, and stimuli beyond this radius suppressed neuronal responses. This suggests that surround suppression for top-down modulation and bottom-up processing occur on similar spatial scales. The same inhibitory circuits could also contribute to decreased receptive field similarity and signal correlation between V1 neurons over ~200 μm (*42*).

38. J. J. Letzkus, S. B. Wolff, E. M. Meyer, P. Tovote, J. Courtin, C. Herry, A. Lüthi, A disinhibitory microcircuit for associative fear learning in the auditory cortex. *Nature* **480**, 331–335 (2011). [Medline](#) [doi:10.1038/nature10674](#)

39. X. Jiang, G. Wang, A. J. Lee, R. L. Stornetta, J. J. Zhu, The organization of two new cortical interneuronal circuits. *Nat. Neurosci.* **16**, 210–218 (2013). [Medline](#) [doi:10.1038/nn.3305](#)

40. S. P. Mysore, E. I. Knudsen, A shared inhibitory circuit for both exogenous and endogenous control of stimulus selection. *Nat. Neurosci.* **16**, 473–478 (2013). [Medline](#) [doi:10.1038/nn.3352](#)

41. S. Ardid, X. J. Wang, A. Compte, An integrated microcircuit model of attentional processing in the neocortex. *J. Neurosci.* **27**, 8486–8495 (2007). [Medline](#) [doi:10.1523/JNEUROSCI.1145-07.2007](#)

42. V. Bonin, M. H. Histed, S. Yurgenson, R. Clay Reid, Local diversity and fine-scale organization of receptive fields in mouse visual cortex. *J. Neurosci.* **31**, 18506 (2011).

43. M. L. Andermann, A. M. Kerlin, R. C. Reid, Chronic cellular imaging of mouse visual cortex during operant behavior and passive viewing. *Front. Cell. Neurosci.* **4**, 3 (2010). Medline

44. D. Green, J. Swets, *Signal Detection Theory and Psychophysics* (J. Wiley, New York, 1966).

45. S. Zhao, J. T. Ting, H. E. Atallah, L. Qiu, J. Tan, B. Gloss, G. J. Augustine, K. Deisseroth, M. Luo, A. M. Graybiel, G. Feng, Cell type–specific channelrhodopsin-2 transgenic mice for optogenetic dissection of neural circuitry function. *Nat. Methods* **8**, 745–752 (2011). Medline doi:10.1038/nmeth.1668

46. B. K. Lim, K. W. Huang, B. A. Grueter, P. E. Rothwell, R. C. Malenka, Anhedonia requires MC4R-mediated synaptic adaptations in nucleus accumbens. *Nature* **487**, 183–189 (2012). Medline doi:10.1038/nature11160

47. N. R. Wall, I. R. Wickersham, A. Cetin, M. De La Parra, E. M. Callaway, Monosynaptic circuit tracing in vivo through Cre-dependent targeting and complementation of modified rabies virus. *Proc. Natl. Acad. Sci. U.S.A.* **107**, 21848–21853 (2010). Medline doi:10.1073/pnas.1011756107

48. N. Maheshri, J. T. Koerber, B. K. Kaspar, D. V. Schaffer, Directed evolution of adeno-associated virus yields enhanced gene delivery vectors. *Nat. Biotechnol.* **24**, 198–204 (2006). Medline doi:10.1038/nbt1182

49. K. Miyamichi, F. Amat, F. Moussavi, C. Wang, I. Wickersham, N. R. Wall, H. Taniguchi, B. Tasic, Z. J. Huang, Z. He, E. M. Callaway, M. A. Horowitz, L. Luo, Cortical representations of olfactory input by trans-synaptic tracing. *Nature* **472**, 191–196 (2011). Medline doi:10.1038/nature09714

50. F. Osakada, E. M. Callaway, Design and generation of recombinant rabies virus vectors. *Nat. Protoc.* **8**, 1583–1601 (2013). Medline doi:10.1038/nprot.2013.094

51. S. W. Oh, J. A. Harris, L. Ng, B. Winslow, N. Cain, S. Mihalas, Q. Wang, C. Lau, L. Kuan, A. M. Henry, M. T. Mortrud, B. Ouellette, T. N. Nguyen, S. A. Sorensen, C. R. Slaughterbeck, W. Wakeman, Y. Li, D. Feng, A. Ho, E. Nicholas, K. E. Hirokawa, P. Bohn, K. M. Joines, H. Peng, M. J. Hawrylycz, J. W. Phillips, J. G. Hohmann, P. Wohnoutka, C. R. Gerfen, C. Koch, A. Bernard, C. Dang, A. R. Jones, H. Zeng, A mesoscale connectome of the mouse brain. *Nature* **508**, 207–214 (2014). Medline doi:10.1038/nature13186